

---

## **SKI PERSPECTIVE**

### **How this project has contributed to SKI's research goals**

The overall goals for SKI research are:

- to give a basis for SKI 's supervision
- to maintain and develop the competence and research capacity within areas which are important to reactor safety
- to contribute directly to the Swedish safety work.

Above all, this project has contributed to the strategical research goal of competence and research capacity by building up competence within the Department of Reactor Physics at Chalmers University of Technology regarding reactor physics, reactor dynamics and noise diagnostics. The project has also contributed to the research goal of giving a basis for SKI's supervision by developing methods for identification and localization of perturbations in reactor cores.

The report comprises stage 7 of a long-term research and development program. The results have been published in international journals and have been included in both licentiate- and doctor's degrees.

### **Project information:**

<i>Project manager:</i>	Ninos Garis, Department of Reactor Technology, SKI
<i>Project number:</i>	14.5-000983-00156
<i>Previous reports:</i>	SKI report 95:14 (1995), 96:50 (1996), 97:31 (1997), 98:25 (1998), 99:33 (1999), 00:28 (2000).

---

# **Research and Development Program in Reactor Diagnostics and Monitoring with Neutron Noise Methods: Stage 7**

## **Summary**

This report gives an account of the work performed by the Department of Reactor Physics, Chalmers University of Technology, in the frame of a research contract with the Swedish Nuclear Power Inspectorate (SKI), contract No. 14.5-000983-00156. The present report is based on work performed by Imre Pázsit (project leader), Christophe Demazière, Vasilij Arzhanov and Ninos Garis, SKI.

This report constitutes stage 7 of a long-term research and development program concerning the development of diagnostics and monitoring methods for nuclear reactors. The long-term goals are elaborated in more detail in e.g. the Final Reports of stage 1 and 2 (SKI Rapport 95:14 and 96:50, Refs. [1] and [2]). Results up to stage 6 were reported in [1] - [6]. A proposal for the continuation of this program in stage 8 is also given at the end of the report.

The program executed in stage 7 consists of three parts and the work performed in each part is summarized below.

### **Development of a 2-D 2-group neutron noise simulator**

In stage 6, the basic principles of a 3-D fully coupled neutronic/thermal-hydraulic simulator in the frequency domain were presented. The neutronic model relied on the two-group diffusion approximation, whereas the thermal-hydraulic algorithms relied on the so-called “lumped” model. The key element of this simulator was that only the static data were required which could be obtained from the Studsvik Scandpower CASMO-4/TABLES-3/SIMULATE-3 code package.

The simulator was developed with this underlying idea, which means that the calculation of the static fluxes and the eigenvalue were avoided. Depending on what kind of spatial discretization scheme which is used in the noise simulator to calculate the “leakage” noise, it is not granted that the system remains critical by using the group constants supplied by SIMULATE. Nevertheless, when the system is critical, the balance equations should be fulfilled in all nodes with respect to the discretization scheme used. In concrete terms, the calculation of the static fluxes and eigenvalue can be avoided if the system is brought back to criticality by modifying the cross-sections so that the balance equations are always fulfilled with the chosen spatial discretization scheme.

This approach was used in this study with the finite difference scheme. As pointed out in stage 6, the finite difference scheme is relatively inefficient compared to finite elements or nodal methods, but on the other hand it is rather easy to implement. These two more sophisticated schemes are planned to be investigated at a later stage, but for the time being the simulator relying on the finite difference scheme was improved as much as possible so that a 2-D entirely neutronic model could be used for routine calculations. Such a simplified model has plenty of applications, both theoretical and practical ones.

Therefore, much emphasis was put in this stage on the calculational efficiency of the noise simulator. The CPU time was reduced by a factor 15 and the required memory by a factor 8, compared to the previous version. Benchmarking of this noise simulator showed that the level of accuracy on the flux noise (both its amplitude and its phase) is excellent for

all noise source types. However, these comparisons were made for homogeneous systems since these are the only systems for which analytical solutions can be determined. It is expected that the accuracy could deteriorate for heterogeneous systems. Thus a need remains to use a more efficient spatial discretization scheme than the finite difference one.

### **Application of the neutron noise simulator to anomaly localisation**

The 2-D 2-group noise simulator calculates the neutron noise induced by any type of noise source, spatially distributed or not (i.e. localised). It can also be used in an inversion task; the neutron noise can be used as input parameter to an algorithm which determines the location of the corresponding noise source. Such a localisation task was previously developed by Karlsson and Pázsit ([14], [15]).

In this stage, the localisation algorithm was improved since the 2-D 2-group neutron noise simulator was used for the calculation of the transfer function, as opposed to the transfer function corresponding to a homogeneous system as in [14] and [15]. At that time, this means that any realistic core can be studied via this algorithm. It was shown, through simulations, that the localisation procedure located the noise source successfully as long as only one noise source existed in the core. If several noise sources are present simultaneously, selecting a few detectors around a region where one of the noise sources is assumed to be found allows locating this specific noise source properly. Another interesting feature of this improved localisation procedure is that the algorithm is less sensitive to the extraneous background noise, probably due to the fact that the removal cross-section noise to neutron noise transfer function was used in the noise simulator. This was not possible to perform in the previous algorithm that only used one-group theory.

Finally, the localisation algorithm was applied to the Forsmark 1 channel instability event monitored in January 1997 during fuel cycle 16. By selecting a proper set of detectors, the noise source was located close to a fuel element that was discovered to be unseated. Nevertheless, selecting different detector combinations give also sometimes different results, which suggests that there were several simultaneous noise sources in the Forsmark 1 case.

### **Wavelet analysis of Oskarshamn 2 data for detector tube impacting**

Detection of impacting of detector tubes, also called instrument strings, have been a matter of interest both in Swedish and foreign BWRs. Although detection of the vibrations is relatively simple, the discovery and quantification of the severity of impacting is far more complicated. No single method exists that gives absolute results without calibration or comparison with reference measurements.

Most known methods, frequently applied in the past require comparison with a reference, i.e. impacting-free state, such as the broadening of the peak, decreasing of the decay ratio, or distortion of the probability distribution function. However, some time ago wavelet analysis was tried to detect and quantify impacting on an absolute basis, i.e. without the need for calibration ([3], [23]). In that early work a simple wavelet, the Haar wavelet transform was used. The objective of the recent research was to continue this work with two extensions. The first was to test the method on measurements, taken in Oskarshamn 2 during three fuel cycles by GSE Power Systems AB. For these measurements, damage of some vibrating tubes was registered during refuelling. Thus, these data lend an excellent possibility to test any method for detecting impacting. The

second extension was to test other wavelet transforms than the Haar wavelet, to see if there exists a waveform that is more effective in the detection of impacting.

Due to the large amount of data to be processed, in this stage only the first extension could be investigated. A thorough investigation of all measurements was made with the Haar wavelet method. This report gives a complete presentation of these investigations. A good correlation was found between the most severely impacting tubes and the wavelet results. The extension of the investigations to other wavelet forms was left to the next stage.

# **Forskningsprogram angående härddiagnostik och härdövervakning med neutronbrusmetoder: Etapp 7**

## **Sammanfattning**

Denna rapport redovisar det arbete som utförts inom ramen för ett forskningskontrakt mellan Avdelningen för Reaktor fysik, Chalmers tekniska högskola och Statens Kärnkraftinspektion (SKI), kontrakt Nr. 14.5-000983-00156. Rapporten är baserad på arbetsinsatser av Imre Pázsit (projektledare), Christophe Demazière, Vasilij Arzhanov och Ninos Garis (SKI).

Rapporten omfattar etapp 7 i ett långsiktigt forsknings- och utvecklingsprogram angående utveckling av diagnostik och övervakningsmetoder för kärnkraftreaktorer. De långsiktiga målen med programmet har utarbetats i slutrapporterna för etapp 1 och 2 (SKI Rapport 95:14 och 96:50, Ref. [1] och [2]). Uppnådda resultat fram till etapp 6 har redovisats i referenserna [1] - [6]. Ett förslag till fortsättning av programmet i etapp 8 redovisas i slutet av rapporten.

Det utförda forskningsarbetet i etapp 7 består av tre olika delar och arbetet i varje del sammanfattas nedan.

### **Utveckling av en 2-D 2-grupp neutronbrusimulator**

I etapp 6 utarbetades grundprinciperna för en tredimensionell simulator i frekvensdomänen med full koppling mellan neutronik/termohydraulik. Neutronmodellen var baserad på tvågrupps-diffusions approximationen, medan de termohydrauliska algoritmerna använde sig av den så kallade "lumped" modellen. En viktig egenskap för denna simulator var enbart statistiska värden behövdes som indata, vilka kunde erhållas från koderna CASMO-4/TABLES-3/SIMULATE-3 från Studsvik Scandpower.

Simulatorn utvecklades med beaktande av denna idé, vilket i princip betydde att simulatorn inte behövde användas för att beräkna de statistiska flödestätheterna och egenvärdena. Å andra sidan, beroende på vilket diskretiseringsschema man använder i simulatorn för att hantera utläckage, är det inte garanterat att systemet förblir kritiskt med detta förfarande om man använder gruppkonstanterna från SIMULATE i brussimulatorn. Kriticitet hos det statistiska systemet i brussimulatorn är mycket viktigt för en korrekt beskrivning av dynamik vid låga frekvenser. När systemet är kritiskt, måste balansekvationerna vara uppfyllda i alla noder enligt det diskretiseringsschema som används. I synnerhet kan beräkning av de statistiska flödestätheterna och egenvärdet undvikas om systemet återföres till kriticitet genom en modifiering av tvärsnitten så att balansekvationerna i diskretiseringsschemat är uppfyllda.

Denna metod användes i den föreliggande studien med finitdifferensschemat. Som påpekades i etapp 6 är finitdifferensschemat relativt ineffektivt jämfört med finita element metoden eller med de nodala metoderna; å andra sidan är det enkelt att implementera. Vi planerar att undersöka de ovannämnda två mera komplicerade scheman i ett senare skede, men för närvarande har vi förbättrat finitdifferensschemat så mycket som möjligt så att en tvådimensionell, enbart neutronbaserad, modell kunde användas för rutinmässiga beräkningar. En sådan, någorlunda enkel, modell kan användas för ett stort antal potentiella tillämpningar, både teoretiska och praktiska.

Följaktligen har vi lagt ner mycket arbete i denna etapp på den beräkningsmässiga effektiviteten av brussimulatorn. Snabbheten ökades med en faktor 15, och minnesåtgången

minskades med en faktor 8, jämfört med den föregående versionen. Ett test av denna brussimulator visade att noggrannheten i beräkningen för såväl amplitud som fas hos bruset är utmärkt oavsett typ av bruskälla. Dessa tester utfördes för homogena system, eftersom analytiska lösningar enbart kan erhållas för sådana fall. Man kan förvänta sig att noggrannheten skulle kunna försämrats för heterogena system. Detta betyder samtidigt att det kvarstår ett behov av att använda ett mer effektivt rums-diskretiseringsschema än finita differens metoden.

### **Tillämpning av brussimulatore för lokalisering av en anomali**

Brussimulatore beräknar neutronbruset i två dimensioner med tvågruppsteori, framkallad av en bruskälla med en i princip godtycklig rumsfördelning. Den kan även användas i en så kallad invers uppgift, nämligen i en algoritm som använder neutronbruset som indata och bestämmer positionen av en lokaliserad bruskälla. En sådan lokaliseringsskript har utarbetats tidigare av Karlsson och Pázsit ([14], [15]).

I föreliggande etapp har denna lokaliseringsskript förbättrats i och med att 2-D 2-grupps brussimulatore har använts för beräkning av överföringsfunktionen mellan bruskälla och neutronbrus, till skillnad från överföringsfunktionen motsvarande ett homogent system och engruppsteori som det var fallet i [14] och [15]. Detta betyder samtidigt att den nuvarande algoritmen kan användas även för beräkning av realistiska härdar. Genom simuleringar har vi visat att algoritmen lokaliserar bruskällan korrekt så länge det enbart finns en bruskälla i härdan. Om flera lokal bruskällor är aktiva samtidigt, kan man lokalisera varje bruskälla separat genom att använda signaler från ett fåtal detektorer som förmodas omge bruskällan ifråga, istället för att använda alla detektorer. En annan intressant egenskap hos den förbättrade algoritmen är att den är avsevärt mindre känslig för störningar såsom bakgrundsbrus. Anledningen är att i den nuvarande proceduren utgörs bruskällan av fluktuationer av svinn-tvårsnittet, vilka leder till en större lokal komponent än i bruset orsakat av fluktuationer av absorptionstvårsnittet. I den tidigare algoritmen gick det inte använda removalstvårsnittet eftersom den var baserad på engruppsteori.

Slutligen har lokaliseringsskripten använts för lokalisering av kanalinstabiliteten som uppstod i Forsmark 1 i januari 1997 under bränslecykel 16. Genom att välja ett lämpligt antal detektorer har bruskällan (kanalinstabiliteten) lokaliserats i närheten av en bränslepatron som befanns vara osätad under påföljande revision. Emellertid gav val av andra detektorer annorlunda resultat, vilket gör det sannolikt att det fanns flera aktiva bruskällor samtidigt i Forsmark 1 fallet.

### **Wavelet analys av Oskarshamn 2 data för upptäckt av nötning från vibrerande detektorsonder**

Fenomenet med mekaniska stötar (impacting) av detektorsonder mot bränsleboxar har varit föremål för undersökningar både i svenska och utländska kokvattenreaktorer. Medan upptäckt av sondvibrationer är relativt enkelt, är upptäckt och kvantifiering av stötar avsevärt mer komplicerat. Det finns inte någon enskild metod som ger resultat i absoluta termer, utan existerande metoder behöver kalibreras eller jämföras med referensmätningar.

De flesta kända metoderna som hittills har tillämpats kräver jämförelse med en referens, dvs mätdata från vibrationer utan stötar. Metoderna omfattar breddning av vibrationstoppen i effektspektra, minskning av dämpkvoten, eller en förändring ("förvridning") av sannolikhetsfördelningen m m. Sedan en tid har emellertid

waveletsanalys prövats för upptäckt och kvantifiering av stötar på ett absolut sätt, dvs utan behov av kalibrering ([3], [23]). I detta tidigare arbete har vi använt en enkel typ av wavelet, den så kallade Haar wavelet transformen. Målet med föreliggande arbete har varit en fortsättning och utvidgning av dessa undersökningar inom två områden. För det första kan metoden testas på mätningar gjorda i Oskarshamn 2 under tre bränslecykler av GSE Power Systems AB. Till dessa mätningar har man även registrerat skador och nötning av vissa sonder under revisionerna. Därmed ger dessa mätdata en utmärkt möjlighet för att testa olika algoritmer för upptäckt av mekaniska stötar. För det andra kan man testa även andra typer av wavelet transform än Haar-transformen, för att undersöka om det finns andra typer som är mer effektiva för upptäckt av mekanisk påverkan.

P g a den stora mängden data, har vi i denna etapp enbart kunnat genomföra den första av de två ovannämnda utvidgningarna av wavelet-metoden. Detta betyder att vi har genomfört en omfattande undersökning av alla mätningar från Oskarshamn 2 med Haar-metoden. Denna rapport ger en fullständig beskrivning av dessa undersökningar. För de sonder som har varit mest utsatta för stötar har vi hittat en bra överensstämmelse mellan waveletanalysens resultat och de verkliga skador som man observerat vid inspektionerna. Utvidgningen av undersökningarna till andra typ av wavelet lämnats till nästa etapp.

# Section 1

## Development of a 2-D 2-group neutron noise simulator

### 1.1 Introduction

In stage 6, a 2-group neutron noise simulator, based on the diffusion approximation, was presented [6]. This neutron simulator included also a thermal-hydraulic model, the so-called lumped model, which allowed taking both the fuel temperature and the coolant temperature noise into account. The main advantage of the simulator was its ability to handle any realistic core, since all the necessary data were the static data that could be obtained by using the CASMO-4/TABLES-3/SIMULATE-3 code package from Studsvik Scandpower ([7] - [9]).

The aim of the previous study was to prove that elaboration of such a coupled neutronic/thermal-hydraulic noise simulator was possible, and to highlight the most important features of the code. Nevertheless, it appeared that the spatial discretization scheme used in that study, the so-called finite difference scheme, was not very well adapted to the 3-D calculations of a heterogeneous core. The reason is obviously the relatively poor accuracy of the finite difference scheme for heterogeneous systems when the number of nodes is not too large. Increasing the number of nodes would allow coping with this problem, but the calculational time would unfortunately become prohibitively large. Consequently, it was concluded that using a more sophisticated calculational scheme than the finite difference one was required. The Reactor Physics Department, Chalmers University of Technology has now access to FEMLAB, a multiphysics code based on the finite elements method ([10] and [11]), and plans to study the possibility of using it for the neutron noise simulator. Nodal methods are also considered.

Although the use of a more efficient discretization scheme appears to be absolutely necessary, it was decided to develop a somehow simplified model of the neutron noise simulator for very specific qualitative tasks. In this model (still relying on the finite difference scheme), only the neutronic model is used and the user is able to estimate the corresponding flux noise from any noise source located in the core. All the user needs to do is to define a set of cross-sections, representative of the core, and define the location, strength, and types of noise sources present in the core. Such a qualitative model could already have many practical applications, such as the localisation of anomalies in a reactor from the detector readings (see Section 2), or more theoretical applications such as the evaluation of the Moderator Temperature Coefficient (MTC) of reactivity assuming different shapes/strengths/correlations of the noise sources.

Therefore, the previous simplified model was significantly improved regarding its calculational efficiency and its ease to use. In the following, the neutronic model of the simulator is described in more detail compared to the previous report (see [6]) and benchmarked for different kinds of noise sources.

### 1.2 Neutron noise simulator

The neutronic model of the noise simulator relies on the two-group diffusion approximation. All calculations are performed in the frequency domain directly, which is equivalent to define complex cross-sections. The main advantages of using the frequency domain instead of the time domain are twofold. First, it is common practice to use the

Fourier transform of the measured signals. Second, because of the Fourier transform, the time derivative in the equations is eliminated. There is consequently no need to properly choose a time discretization which allows taking into account the phenomena one wants to study, and for which the neutron noise has to be evaluated at each time step. In the frequency domain instead, the calculation needs only to be performed once, assuming that the frequency of interest is known. If not, scanning a frequency range does not appear to be a big burden. Finally, the spatial discretization is carried out by using a finite difference scheme.

### Neutron noise in the 2-group diffusion approximation

In the two-group diffusion approximation, the time- and space-dependent flux can be expressed as follows:

$$\begin{aligned} \frac{1}{v_1} \frac{\partial \phi_1}{\partial t}(\mathbf{r}, t) &= D_1(\mathbf{r}, t) \nabla^2 \phi_1(\mathbf{r}, t) + v \Sigma_{f,2}(\mathbf{r}, t) (1 - \beta_{eff}) \phi_2(\mathbf{r}, t) + \lambda C(\mathbf{r}, t) \\ &+ [v \Sigma_{f,1}(\mathbf{r}, t) (1 - \beta_{eff}) - \Sigma_{a,1}(\mathbf{r}, t) - \Sigma_{rem}(\mathbf{r}, t)] \phi_1(\mathbf{r}, t) \end{aligned} \quad (1)$$

and

$$\frac{1}{v_2} \frac{\partial \phi_2}{\partial t}(\mathbf{r}, t) = D_2(\mathbf{r}, t) \nabla^2 \phi_2(\mathbf{r}, t) - \Sigma_{a,2}(\mathbf{r}, t) \phi_2(\mathbf{r}, t) + \Sigma_{rem}(\mathbf{r}, t) \phi_1(\mathbf{r}, t) \quad (2)$$

with the precursor density given as:

$$\frac{\partial C}{\partial t}(\mathbf{r}, t) = \beta_{eff} [v \Sigma_{f,1}(\mathbf{r}, t) \phi_1(\mathbf{r}, t) + v \Sigma_{f,2}(\mathbf{r}, t) \phi_2(\mathbf{r}, t)] - \lambda C(\mathbf{r}, t) \quad (3)$$

Assuming that all the time-dependent parameters can be expressed as:

$$X(\mathbf{r}, t) = X_0(\mathbf{r}) + \delta X(\mathbf{r}, t) \quad (4)$$

where the index 0 represents the static case, subtracting the static case to Eqs. (1)-(3), performing a temporal Fourier transform and neglecting the second-order terms lead to the following matrix formulation:

$$\begin{aligned} &(\bar{\bar{D}}(\mathbf{r}) \nabla^2 + \bar{\bar{\Phi}}(\mathbf{r}, \omega)) \begin{bmatrix} \delta \phi_1(\mathbf{r}, \omega) \\ \delta \phi_2(\mathbf{r}, \omega) \end{bmatrix} \\ &= \bar{\bar{\Sigma}}_{rem}(\mathbf{r}) \delta \Sigma_{rem}(\mathbf{r}, \omega) + \bar{\bar{\Sigma}}_a(\mathbf{r}) \begin{bmatrix} \delta \Sigma_{a,1}(\mathbf{r}, \omega) \\ \delta \Sigma_{a,2}(\mathbf{r}, \omega) \end{bmatrix} + \bar{\bar{\Sigma}}_f(\mathbf{r}, \omega) \begin{bmatrix} \delta v \Sigma_{f,1}(\mathbf{r}, \omega) \\ \delta v \Sigma_{f,2}(\mathbf{r}, \omega) \end{bmatrix} \end{aligned} \quad (5)$$

where the different matrices are given as:

$$\bar{\bar{D}}(\mathbf{r}) = \begin{bmatrix} D_1(\mathbf{r}) & 0 \\ 0 & D_2(\mathbf{r}) \end{bmatrix} \quad (6)$$

$$\bar{\bar{\phi}}(\mathbf{r}, \omega) = \begin{bmatrix} -\Sigma_1(\mathbf{r}, \omega) \nu \Sigma_{f,2}(\mathbf{r}, \omega) \\ \Sigma_{rem,0}(\mathbf{r}) - \Sigma_{a,2}(\mathbf{r}, \omega) \end{bmatrix} \quad (7)$$

$$\bar{\bar{\Sigma}}_{rem}(\mathbf{r}) = \begin{bmatrix} \phi_{1,0}(\mathbf{r}) \\ -\phi_{1,0}(\mathbf{r}) \end{bmatrix} \quad (8)$$

$$\bar{\bar{\Sigma}}_a(\mathbf{r}) = \begin{bmatrix} \phi_{1,0}(\mathbf{r}) & 0 \\ 0 & \phi_{2,0}(\mathbf{r}) \end{bmatrix} \quad (9)$$

$$\bar{\bar{\Sigma}}_f(\mathbf{r}, \omega) = \begin{bmatrix} -\phi_{1,0}(\mathbf{r}) \left(1 - \frac{i\omega\beta_{eff}}{i\omega + \lambda}\right) & -\phi_{2,0}(\mathbf{r}) \left(1 - \frac{i\omega\beta_{eff}}{i\omega + \lambda}\right) \\ 0 & 0 \end{bmatrix} \quad (10)$$

and the different coefficients are defined as:

$$\Sigma_1(\mathbf{r}, \omega) = \Sigma_{a,1,0}(\mathbf{r}) + \frac{i\omega}{v_1} + \Sigma_{rem,0}(\mathbf{r}) - \nu \Sigma_{f,1,0}(\mathbf{r}) \left(1 - \frac{i\omega\beta_{eff}}{i\omega + \lambda}\right) \quad (11)$$

$$\nu \Sigma_{f,2}(\mathbf{r}, \omega) = \nu \Sigma_{f,2,0}(\mathbf{r}) \left(1 - \frac{i\omega\beta_{eff}}{i\omega + \lambda}\right) \quad (12)$$

$$\Sigma_{a,2}(\mathbf{r}, \omega) = \Sigma_{a,2,0}(\mathbf{r}) + \frac{i\omega}{v_2} \quad (13)$$

From Eq. (5), it is obvious that the right-hand-side represents the neutron noise source. Compared to the calculation of the static neutron flux (which is an eigenvalue problem), the estimation of the neutron noise is a simpler task since there is no need to iterate on the fission term. The only difficulty lies with the fact that Eq. (5) uses complex cross-sections, as the ones defined by Eqs. (11)-(13). These cross-sections are frequency-dependent. This means that a new set of calculation has to be performed for each frequency that one might consider.

## 2-D spatial discretization

Due to the  $\nabla^2$  operator in Eq. (5), a spatial discretization scheme has to be chosen. The finite difference scheme was retained for its simplicity and its efficiency. As will be shown in §1.3, this scheme is satisfactory for homogeneous systems. Nevertheless, it is known that the number of nodes needs to be increased significantly in heterogeneous systems, if one wants to obtain an acceptable level of accuracy. Therefore, other more powerful

discretization schemes, such as nodal methods or finite elements, will be considered at a later stage.

The starting point of the discretization procedure is the integration of Eq. (5) over an elementary volume. The unknowns are thus expressed by the following generic formulation:

$$\delta X_{I,J}(\omega) = \frac{1}{\Delta x \cdot \Delta y} \int_{(I,J)} \delta X(\mathbf{r}, \omega) d\mathbf{r} \quad (14)$$

whereby the elements of the matrices satisfy the following relationship:

$$m_{I,J}(\omega) \delta X_{I,J}(\omega) = \frac{1}{\Delta x \cdot \Delta y} \int_{(I,J)} m(\mathbf{r}, \omega) \delta X(\mathbf{r}, \omega) d\mathbf{r} \quad (15)$$

$$\Leftrightarrow m_{I,J}(\omega) = \frac{\int_{(I,J)} m(\mathbf{r}, \omega) \delta X(\mathbf{r}, \omega) d\mathbf{r}}{\int_{(I,J)} \delta X(\mathbf{r}, \omega) d\mathbf{r}}$$

This way of averaging is consistent with the two-group constants provided by any static core calculator, so that the actual reaction rates are preserved.

If one represents a node  $I,J$  by the system of axes and numbering as shown in Fig. 1, the spatial discretization of the neutron noise can be carried out according to the ‘‘box-scheme’’ that allows writing [12]:

$$\begin{aligned} & \frac{1}{\Delta x \cdot \Delta y} \int_{(I,J)} D_{\Delta\delta\phi} \nabla^2 \delta\phi(\mathbf{r}, \omega) d\mathbf{r} \\ &= - \frac{[\delta J_{I,J}^x(\omega) - \delta J_{I-1,J}^x(\omega)]}{\Delta x} - \frac{[\delta J_{I,J}^y(\omega) - \delta J_{I,J-1}^y(\omega)]}{\Delta y} \end{aligned} \quad (16)$$

For each direction (either the  $x$  or  $y$  direction), two expressions for the current noise  $\delta J(\omega)$  can be written by considering the node  $I,J$  and its neighbours (either the  $I+1,J$  or  $I,J+1$  node respectively). Equating these two expressions allows eliminating the flux noise at the boundary of the two nodes, so that the current noise can be expressed as directly depending on the node-average flux noise in the node  $I,J$  and the node-average flux noise in its neighbouring nodes. In a given energy-group  $g$ , one obtains:

$$\begin{aligned} & \delta J_{g,I,J}^x(\omega) - \delta J_{g,I-1,J}^x(\omega) \\ &= a_{g,I,J}^x \delta\phi_{g,I,J}(\omega) + b_{g,I,J}^x \delta\phi_{g,I+1,J}(\omega) + c_{g,I,J}^x \delta\phi_{g,I-1,J}(\omega) \end{aligned} \quad (17)$$

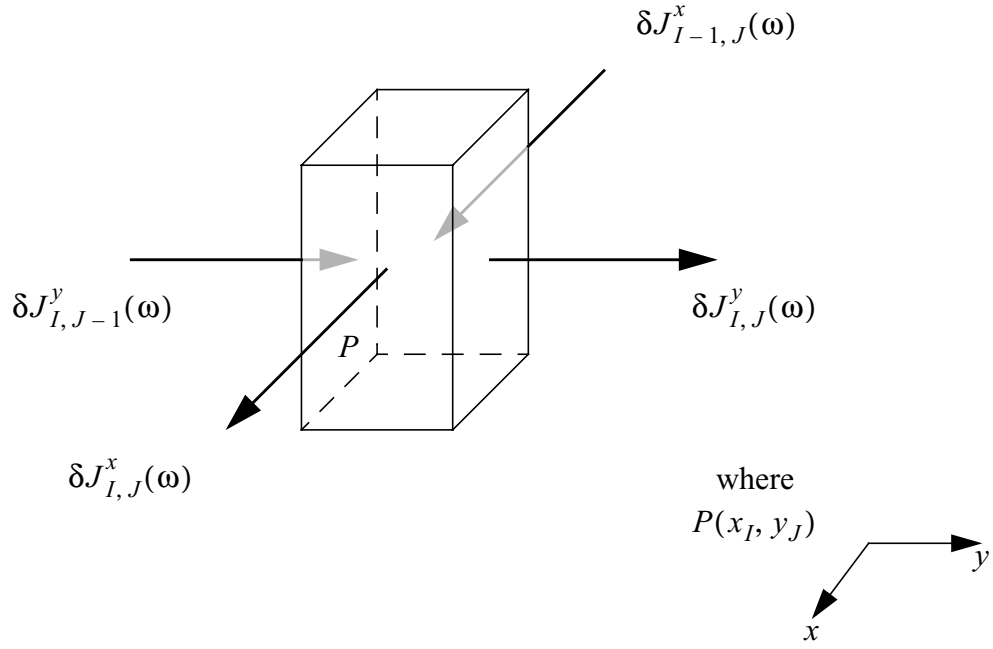


**Fig. 1.** Principles and convention used in the discretisation scheme (2-D case).

$$\begin{aligned}
 & \delta J_{g,I,J}^y - \delta J_{g,I,J-1}^y \\
 & = a_{g,I,J}^y \delta \phi_{g,I,J}(\omega) + b_{g,I,J}^y \delta \phi_{g,I,J+1}(\omega) + c_{g,I,J}^y \delta \phi_{g,I,J-1}(\omega)
 \end{aligned} \tag{18}$$

The different coefficients  $a_{g,I,J}^x$ ,  $a_{g,I,J}^y$ ,  $b_{g,I,J}^x$ ,  $b_{g,I,J}^y$ ,  $c_{g,I,J}^x$ , and  $c_{g,I,J}^y$  are summarised in Table I and Table II for the  $x$  and  $y$  directions, respectively.

**Table I.** Coupling coefficients in the  $x$  direction.

	$a_{g,I,J}^x$	$b_{g,I,J}^x$	$c_{g,I,J}^x$
if the node $I-1$ does not exist	$\frac{2D_{g,I,J}D_{g,I+1,J}}{\Delta x(D_{g,I,J} + D_{g,I+1,J})} + \frac{2D_{g,I,J}}{\Delta x}$	$-\frac{2D_{g,I,J}D_{g,I+1,J}}{\Delta x(D_{g,I,J} + D_{g,I+1,J})}$	0
if the nodes $I-1$ and $I+1$ both exist	$\frac{2D_{g,I,J}D_{g,I+1,J}}{\Delta x(D_{g,I,J} + D_{g,I+1,J})} + \frac{2D_{g,I,J}D_{g,I-1,J}}{\Delta x(D_{g,I,J} + D_{g,I-1,J})}$	$-\frac{2D_{g,I,J}D_{g,I+1,J}}{\Delta x(D_{g,I,J} + D_{g,I+1,J})}$	$-\frac{2D_{g,I,J}D_{g,I-1,J}}{\Delta x(D_{g,I,J} + D_{g,I-1,J})}$
if the node $I+1$ does not exist	$\frac{2D_{g,I,J}}{\Delta x} + \frac{2D_{g,I,J}D_{g,I-1,J}}{\Delta x(D_{g,I,J} + D_{g,I-1,J})}$	0	$-\frac{2D_{g,I,J}D_{g,I-1,J}}{\Delta x(D_{g,I,J} + D_{g,I-1,J})}$

**Table II.** Coupling coefficients in the  $y$  direction.

	$a_{g,I,J}^y$	$b_{g,I,J}^y$	$c_{g,I,J}^y$
if the node $J-1$ does not exist	$\frac{2D_{g,I,J}D_{g,I,J+1}}{\Delta y(D_{g,I,J} + D_{g,I,J+1})} + \frac{2D_{g,I,J}}{\Delta y}$	$\frac{2D_{g,I,J}D_{g,I,J+1}}{\Delta y(D_{g,I,J} + D_{g,I,J+1})}$	0
if the nodes $J-1$ and $J+1$ both exist	$\frac{2D_{g,I,J}D_{g,I,J+1}}{\Delta y(D_{g,I,J} + D_{g,I,J+1})} + \frac{2D_{g,I,J}D_{g,I,J-1}}{\Delta y(D_{g,I,J} + D_{g,I,J-1})}$	$\frac{2D_{g,I,J}D_{g,I,J+1}}{\Delta y(D_{g,I,J} + D_{g,I,J+1})}$	$\frac{2D_{g,I,J}D_{g,I,J-1}}{\Delta y(D_{g,I,J} + D_{g,I,J-1})}$
if the node $J+1$ does not exist	$\frac{2D_{g,I,J}}{\Delta y} + \frac{2D_{g,I,J}D_{g,I,J-1}}{\Delta y(D_{g,I,J} + D_{g,I,J-1})}$	0	$\frac{2D_{g,I,J}D_{g,I,J-1}}{\Delta y(D_{g,I,J} + D_{g,I,J-1})}$

By using Eqs. (14)-(18), the discretised system of equations that has to be solved can be derived from Eq. (5) as follows:

$$\overline{\overline{D}}_{\delta\phi}^{discr}(\omega)\overline{\overline{\delta\phi}}^{discr}(\omega) = \overline{\overline{\Sigma}}_{rem}^{discr}\overline{\overline{\delta\Sigma}}_{rem}^{discr}(\omega) + \overline{\overline{\Sigma}}_a^{discr}\overline{\overline{\delta\Sigma}}_a^{discr}(\omega) + \overline{\overline{\Sigma}}_f^{discr}(\omega)\overline{\overline{\delta v\Sigma}}_f^{discr}(\omega) \quad (19)$$

Whereas the expression of each term on the right-hand-side of Eq. (19) is relatively straightforward, the left-hand-side needs to be clarified a little bit further. If one considers a given node  $I,J$ , one has:

$$\overline{D\delta\phi}^{\text{discr}}(\omega)\overline{\delta\phi}^{\text{discr}}(\omega)]_{(I,J)} \quad (20)$$

$$= \begin{bmatrix} -\Sigma_{1,I,J}(\omega) - \frac{a_{1,I,J}^x}{\Delta x} - \frac{a_{1,I,J}^y}{\Delta y} & v\Sigma_{f,2,I,J}(\omega) \\ \Sigma_{rem,0,I,J} & -\Sigma_{a,2,I,J}(\omega) - \frac{a_{2,I,J}^x}{\Delta x} - \frac{a_{2,I,J}^y}{\Delta y} \end{bmatrix} \times \begin{bmatrix} \delta\phi_{1,I,J}(\omega) \\ \delta\phi_{2,I,J}(\omega) \end{bmatrix}$$

$$+ \begin{bmatrix} \frac{b_{1,I,J}^x}{\Delta x} & 0 \\ 0 & -\frac{b_{2,I,J}^x}{\Delta x} \end{bmatrix} \times \begin{bmatrix} \delta\phi_{1,I+1,J}(\omega) \\ \delta\phi_{2,I+1,J}(\omega) \end{bmatrix} + \begin{bmatrix} \frac{b_{1,I,J}^y}{\Delta x} & 0 \\ 0 & -\frac{b_{2,I,J}^y}{\Delta x} \end{bmatrix} \times \begin{bmatrix} \delta\phi_{1,I,J+1}(\omega) \\ \delta\phi_{2,I,J+1}(\omega) \end{bmatrix}$$

$$+ \begin{bmatrix} -\frac{c_{1,I,J}^x}{\Delta x} & 0 \\ 0 & -\frac{c_{2,I,J}^x}{\Delta x} \end{bmatrix} \times \begin{bmatrix} \delta\phi_{1,I-1,J}(\omega) \\ \delta\phi_{2,I-1,J}(\omega) \end{bmatrix} + \begin{bmatrix} -\frac{c_{1,I,J}^y}{\Delta x} & 0 \\ 0 & -\frac{c_{2,I,J}^y}{\Delta x} \end{bmatrix} \times \begin{bmatrix} \delta\phi_{1,I,J-1}(\omega) \\ \delta\phi_{2,I,J-1}(\omega) \end{bmatrix}$$

The  $\overline{D\delta\phi}^{\text{discr}}(\omega)$  matrix is obviously sparse. If one has a 2-D core with  $N$  nodes, one has  $2N$  unknowns and the matrix is of a  $2N \times 2N$  size. This matrix can be inverted so that the flux noise can be directly expressed as (source problem):

$$\overline{\delta\phi}^{\text{discr}}(\omega) \quad (21)$$

$$= [\overline{D\delta\phi}^{\text{discr}}(\omega)]^{-1} \overline{\Sigma_{rem}}^{\text{discr}} \overline{\delta\Sigma_{rem}}^{\text{discr}}(\omega) + [\overline{D\delta\phi}^{\text{discr}}(\omega)]^{-1} \overline{\Sigma_a}^{\text{discr}} \overline{\delta\Sigma_a}^{\text{discr}}(\omega)$$

$$+ [\overline{D\delta\phi}^{\text{discr}}(\omega)]^{-1} \overline{\Sigma_f}^{\text{discr}}(\omega) \overline{\delta v\Sigma_f}^{\text{discr}}(\omega)$$

## Data required

The only data required by the noise simulator are the static data, i.e. the material constants and the point-kinetic parameters of the core. These data can be easily retrieved from any static core simulator. Nevertheless, there is one particular aspect that is worth mentioning and that could lead to differences in the calculation of the flux noise. Namely, the spatial discretization scheme used to generate the 2-D material constants needs to be in agreement with the one used in the noise simulator.

More specifically, the first necessary step in the estimation of the noise should be the calculation of the static flux and the eigenvalue with the finite difference scheme, i.e. a scheme which is identical with the one used in the noise determination. It is not granted that the flux and eigenvalue given by the finite difference scheme will correspond to the one given by the static core simulator. In such a case, using the static data directly from the static core simulator would be equivalent to make the system non-critical.

Nevertheless, recalculating the static flux and the corresponding eigenvalue with a finite difference scheme is identical to neglect the main advantage of using a commercial core simulator, i.e. its accuracy. This is why another approach was preferred in this study. This approach is simpler since no calculation of the static flux and eigenvalue is required. The static flux of the core simulator is in fact directly used to adjust the static cross-sections so that the balance equations are fulfilled in each node with the finite difference scheme. This is completely equivalent to make the system critical with the most accurate set of fluxes available and with a scheme compatible to the one used in the noise estimation.

The balance equations that need to be fulfilled are given as:

$$[D_1(\mathbf{r})\Delta\phi_1(\mathbf{r})]_{(I,J)} + \frac{v\Sigma_{f,1,I,J}}{k_{eff}}\phi_{1,I,J} + \frac{v\Sigma_{f,2(1),I,J}}{k_{eff}}\phi_{2,I,J} \quad (22)$$

$$- \Sigma_{a,1,I,J}\phi_{1,I,J} - \Sigma_{rem,I,J}\phi_{1,I,J} = 0$$

$$[D_2(\mathbf{r})\Delta\phi_2(\mathbf{r})]_{(I,J)} + \Sigma_{rem,I,J}\phi_{1,I,J} - \Sigma_{a,2,I,J}\phi_{2,I,J} = 0 \quad (23)$$

with the leakage terms estimated according to the finite difference scheme below:

$$D_1(\mathbf{r})\Delta\phi_1(\mathbf{r})]_{(I,J)} = \left( \frac{a_{1,I,J}^x}{\Delta x} + \frac{a_{1,I,J}^y}{\Delta y} \right) \phi_{1,I,J} \quad (24)$$

$$+ \frac{b_{1,I,J}^x}{\Delta x} \phi_{1,I+1,J} + \frac{b_{1,I,J}^y}{\Delta y} \phi_{1,I,J+1} + \frac{c_{1,I,J}^x}{\Delta x} \phi_{1,I-1,J} + \frac{c_{1,I,J}^y}{\Delta y} \phi_{1,I,J-1}$$

$$D_2(\mathbf{r})\Delta\phi_2(\mathbf{r})]_{(I,J)} = \left( \frac{a_{2,I,J}^x}{\Delta x} + \frac{a_{2,I,J}^y}{\Delta y} \right) \phi_{2,I,J} \quad (25)$$

$$+ \frac{b_{2,I,J}^x}{\Delta x} \phi_{2,I+1,J} + \frac{b_{2,I,J}^y}{\Delta y} \phi_{2,I,J+1} + \frac{c_{2,I,J}^x}{\Delta x} \phi_{2,I-1,J} + \frac{c_{2,I,J}^y}{\Delta y} \phi_{2,I,J-1}$$

The following procedure has been applied for the adjustment of the cross-sections used in this study (see §1.3 and Section 2). First, the thermal absorption cross-section was modified to fulfil Eqs. (23) and (25). If such an adjustment was not possible (because it would result in a negative cross-section), the removal cross-section was modified instead, and the eigenvalue modified so that Eqs. (22) and (24) could be fulfilled. If this too was impossible, the fast absorption cross-section could also be modified. For the reflector nodes, an adjustment of the absorption cross-sections (both fast and thermal) is first carried out. In case of negative results, the removal cross-section is modified. But due to the coupling between the fast and thermal groups and the relatively few number of parameters that can be changed, an iterative procedure is required if the removal cross-section is adjusted in the reflector nodes. As a matter of fact, this procedure only affects appreciably the cross-sections in the reflector nodes, and to a lesser extent the cross-sections of the fuel nodes immediately neighbouring the reflector. The main reason lies with the fact that a finite difference scheme does not estimate the static flux accurately in these nodes when only a few nodes are used for the calculation.

## Computational performance

As pointed out previously, the finite difference scheme is easy to implement and use, but requires a huge amount of memory if one wants to have an acceptable level of accuracy. Obviously, increasing the number of nodes is what one tends to do since the accuracy becomes better in such a case.

In stage 6, the noise simulator was based directly on the real core structure, i.e. all the data and calculations were performed by using the actual coordinates of each node in a square core map. Nevertheless, all the nodes located outside the reflector are unrealistic nodes and were eliminated just before inverting the matrix  $\underline{\underline{D}}_{\delta\phi}(\omega)$ . This way of performing the calculations was easy from the user's point of view, since all the data could be defined and checked during the calculations, but inefficient with respect to memory utilisation, since one used more memory than one actually needed. In the new version of the noise simulator, the unrealistic nodes were not used at all. Therefore, instead of eliminating the empty rows and columns of the  $\underline{\underline{D}}_{\delta\phi}(\omega)$  matrix just before its inversion, the unrealistic elements of  $\underline{\underline{D}}_{\delta\phi}(\omega)$  were not defined right from the start. This might appear to be a trivial task, but another way of improving the time required for the calculations is to use the sparsity properties of the matrices and the corresponding tools in MATLAB [13]. The combination of both makes the numbering and the definition of the nodes a difficult and cumbersome task. The structure of the  $\underline{\underline{D}}_{\delta\phi}(\omega)$  matrix is represented in Fig. 2.

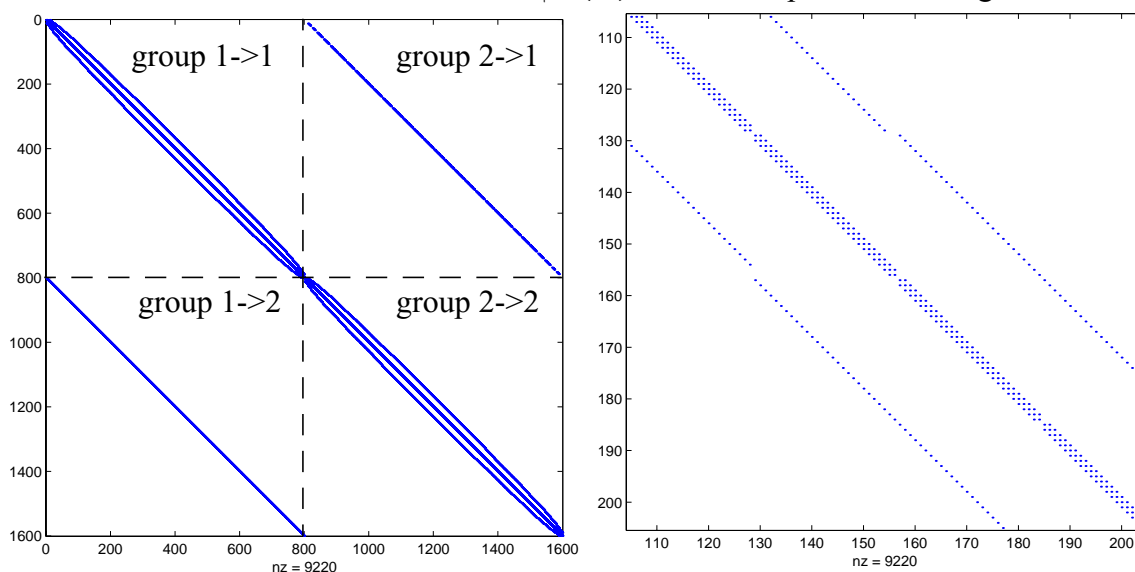


**Fig. 2.** Sparsity of the matrix (full matrix on the left-hand-side, and a closer look at the upper left corner on the right-hand-side)

Obviously, because of the coupling between one node and its neighbours, the main diagonal of the matrix is surrounded by four other “diagonals”, as can be seen on the right-hand side of Fig. 2. These secondary “diagonals” are distorted simply because the core is not square (the unrealistic nodes are not taken into account).

In Table III, the CPU time and memory required for the calculation of the transfer functions for both the previous noise simulator and its new version are compared. As can be seen, it takes now only a few minutes to estimate the transfer function of a typical BWR core with 4 subnodes per assembly. Such a number of subnodes was not even achievable with the previous version. This is mainly due to the fact that the memory needed by the new simulator is significantly reduced compared to the previous one. As can be noticed also, for

a BWR core like Forsmark 1 (676 fuel assemblies + 124 reflector nodes), four subnodes per assembly already correspond to the maximum number of subnodes that the new noise simulator can handle.

**Table III.** Comparison between the old and new versions of the noise simulator

Number of subnodes per assembly	Old version		New version	
1x1	CPU time (s): 651	Memory (Mbytes): 429	CPU time (s): 39	Memory (Mbytes): 51
2x2	CPU time (s): -	Memory (Mbytes): not achievable with a 32-bit code	CPU time (s): 861	Memory (Mbytes): 820
3x3	CPU time (s): -	Memory (Mbytes): not achievable with a 32-bit code	CPU time (s): -	Memory (Mbytes): not achievable with a 32-bit code

Another new feature of the noise simulator is that every core layout, i.e. BWR and PWR cores with different sizes can now be handled. All the user needs to do is to define a core map specifying where the fuel assemblies and the reflector nodes are located. The user also has to provide the corresponding static data (material constants and fluxes defined in maps matching the core map, and the point-kinetic parameters of the core).

### 1.3 Benchmarking of the simulator

Even if the cross-sections need to be adjusted before using the noise simulator, the modifications of these are almost negligible in the fuel nodes. As pointed out previously, only the fuel nodes directly neighbouring the reflector nodes are appreciably modified. Therefore locating a noise source in the middle of the core and assuming that the core is homogeneous for the estimation of an analytical solution should provide a relatively good reference solution for the numerical scheme far away from the reflector nodes.

#### Analytical solution in case of a central noise source

It is assumed in the following that the noise source for the analytical solution is a point source located at the core centre. Three different cases have been considered: a noise source defined in terms of the fluctuation of the fast absorption cross-section, one of the thermal absorption cross-section, and finally one of the removal cross-section. This can be formulated by writing Eq. (5) as follows:

$$(\bar{D}(\mathbf{r})\nabla^2 + \bar{\phi}(\mathbf{r}, \omega)) \begin{bmatrix} \delta\phi_1(\mathbf{r}, \omega) \\ \delta\phi_2(\mathbf{r}, \omega) \end{bmatrix} = \begin{bmatrix} S_1(\mathbf{r}, \omega) \\ S_2(\mathbf{r}, \omega) \end{bmatrix} \quad (26)$$

with the following three possibilities for the noise source:

$$\begin{bmatrix} S_1(\mathbf{r}, \omega) \\ S_2(\mathbf{r}, \omega) \end{bmatrix} = \gamma(\omega) \times \begin{bmatrix} \delta(\mathbf{r})\phi_{1,0}(\mathbf{r}) \\ 0 \end{bmatrix}, \quad (27)$$

or

$$\begin{bmatrix} S_1(\mathbf{r}, \omega) \\ S_2(\mathbf{r}, \omega) \end{bmatrix} = \gamma(\omega) \times \begin{bmatrix} 0 \\ \delta(\mathbf{r})\phi_{2,0}(\mathbf{r}) \end{bmatrix}, \quad (28)$$

or

$$\begin{bmatrix} S_1(\mathbf{r}, \omega) \\ S_2(\mathbf{r}, \omega) \end{bmatrix} = \gamma(\omega) \times \begin{bmatrix} \delta(\mathbf{r})\phi_{1,0}(\mathbf{r}) \\ -\delta(\mathbf{r})\phi_{1,0}(\mathbf{r}) \end{bmatrix}. \quad (29)$$

Here  $\gamma(\omega)$  is the noise source strength. This coefficient allows also taking into account the fact that the noise source is homogeneously distributed over one or several nodes in the numerical solution (the nodes representing the core centre), and therefore is not a point-source.

Due to the symmetry of the system, the flux noise is simply given by:

$$\delta\phi_1(r, \omega) = A \times K_0(\lambda r) + B \times I_0(\lambda r) + C \times Y_0(\mu r) + D \times J_0(\mu r) \quad (30)$$

$$\begin{aligned} \delta\phi_2(r, \omega) & \\ &= A \times c_\lambda \times K_0(\lambda r) + B \times c_\lambda \times I_0(\lambda r) + C \times c_\mu \times Y_0(\mu r) + D \times c_\mu \times J_0(\mu r) \end{aligned} \quad (31)$$

where  $-\lambda^2$  and  $\mu^2$  are the two eigenvalues of the following matrix:

$$\begin{bmatrix} -\Sigma_1(\omega)/D_1 & \nu\Sigma_{f,2}(\omega)/D_1 \\ \Sigma_{rem,0}/D_2 & -\Sigma_{a,2}(\omega)/D_2 \end{bmatrix} \quad (32)$$

and the coupling coefficient  $c_\lambda$  and  $c_\mu$  are given as follows:

$$c_\lambda = \frac{\Sigma_{rem,0}}{\Sigma_{a,2}(\omega) - D_2\lambda^2} \quad (33)$$

$$c_\mu = \frac{\Sigma_{rem,0}}{\Sigma_{a,2}(\omega) + D_2\mu^2} \quad (34)$$

The coefficients  $A$ ,  $B$ ,  $C$ , and  $D$  are solutions of the system:

$$\begin{aligned}
& \begin{bmatrix} K_0(\lambda R) & I_0(\lambda R) & Y_0(\mu R) & J_0(\mu R) \\ c_\lambda \times K_0(\lambda R) & c_\lambda \times I_0(\lambda R) & c_\mu \times Y_0(\mu R) & c_\mu \times J_0(\mu R) \\ -1 & 0 & -[\mu r \times Y_1(\mu r)]_{r \rightarrow 0} & 0 \\ -c_\lambda & 0 & -c_\mu \times [\mu r \times Y_1(\mu r)]_{r \rightarrow 0} & 0 \end{bmatrix} \times \begin{bmatrix} A \\ B \\ C \\ D \end{bmatrix} \quad (35) \\
& = \begin{bmatrix} 0 \\ 0 \\ \frac{1}{2\pi D_1} \int S_1(r, \omega) dr \\ \frac{1}{2\pi D_2} \int S_2(r, \omega) dr \end{bmatrix}
\end{aligned}$$

where  $R$  is the core radius (fuel + reflector zones).

### Comparison between the numerical and analytical solutions

The following figures (see Figs. 3-5) depict the amplitude of the flux noise and its phase for both the analytical solution and the numerical one. Since the noise simulator calculates a spatially-averaged flux noise over each node, the analytical solution was also averaged over each node, so that both solutions could be directly compared. The first point of the numerical solution (from the core centre) represents the flux noise in the node where the noise source is located. The analytical solution gives obviously a different solution in this node, and therefore the first point of the analytical solution was systematically disregarded.

It can be noticed that the agreement between the analytical and the numerical solutions is very good. As expected, the discrepancy is somewhat larger at the core boundary than at the core centre, due to two main reasons. The first one is simply the presence of the reflector in the numerical simulation, whereas the analytical one does not take any reflector into account. The second effect lies with the fact that close to the reflector nodes, the cross-sections have been adjusted in the noise simulator, so that the system remains critical despite the use of the finite difference scheme. Therefore, while in the analytical case the reactor is homogeneous, the core becomes more and more heterogeneous close to the core boundary in the numerical case. Since the flux noise vanishes at the core boundary, the difference between the analytical and numerical solutions is hardly noticeable for the amplitude of the noise. Even if the discrepancy regarding the phase of the flux noise slightly increases away from the core centre, the accuracy still remains very good, as can be seen on the different Figures.

Consequently, the noise simulator seems to reproduce the expected solution rather well. Despite the apparent high level of accuracy, the fact that the core is homogeneous (or more exactly almost homogeneous) has to be strongly emphasized. The finite difference scheme is a very effective (and easy to implement) discretization scheme as long as the discretised system does not present a strong level of heterogeneity. A realistic core is of course far from being homogeneous. Even if core homogeneity is still an acceptable approximation for PWRs, BWRs are highly heterogeneous systems due to the presence of

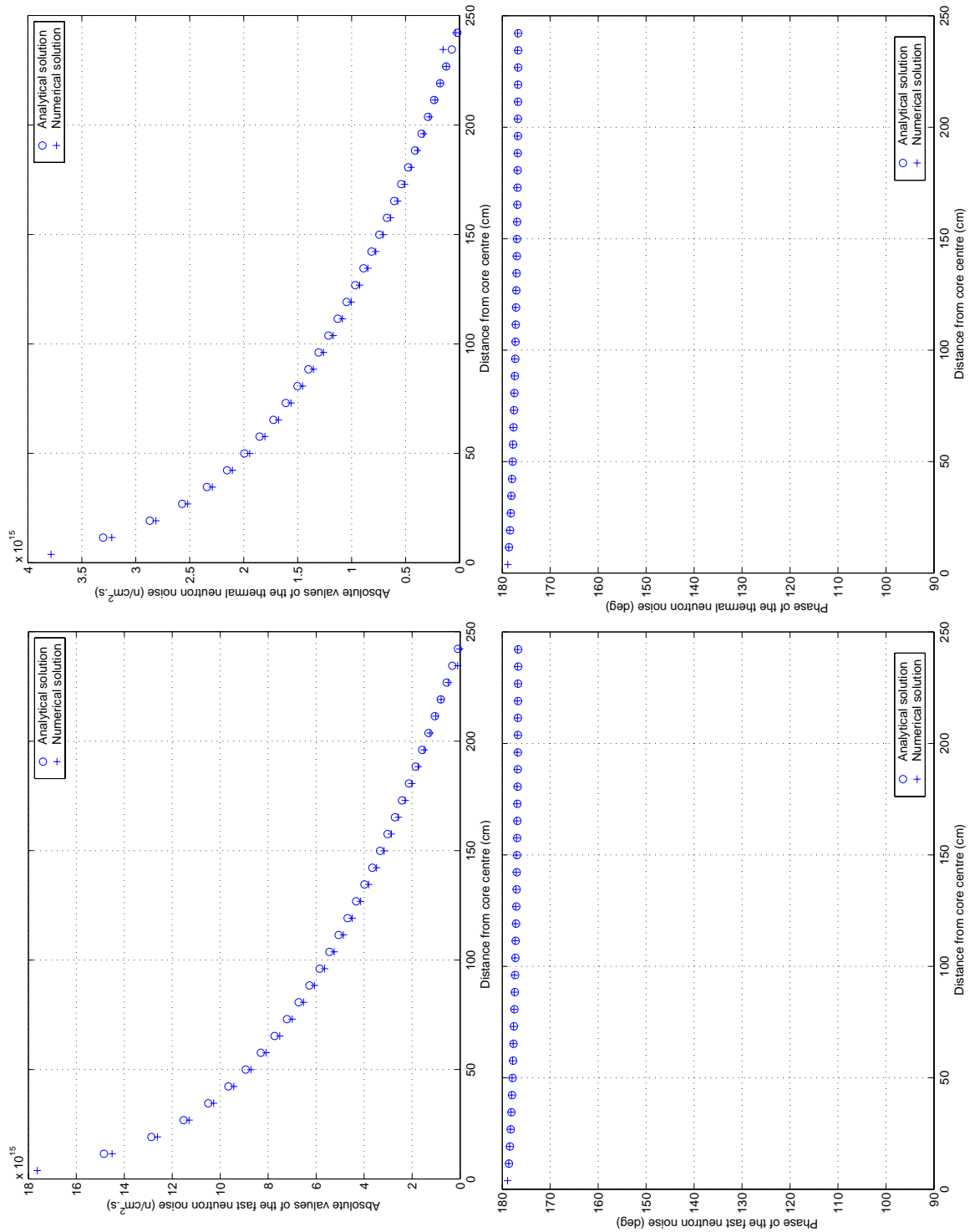


**Fig. 3.** Comparison between the analytical and numerical solutions, for the case of a fast absorption cross-section noise source

the control rods (in a PWR, the reactivity adjustment is mainly carried out by the boron concentration). Therefore, the accuracy may deteriorate appreciably when a realistic core is modelled. One way of coping with this could be to increase the number of nodes in the numerical simulation. Nevertheless, a commercial BWR like Forsmark 1 has already 800 nodes in the radial direction (676 fuel assemblies + 124 reflector nodes). As pointed out previously, the corresponding matrix representing the transfer function is of a 1600x1600 size. Dividing each node into 4 sub-nodes is still possible, but already appears to be the

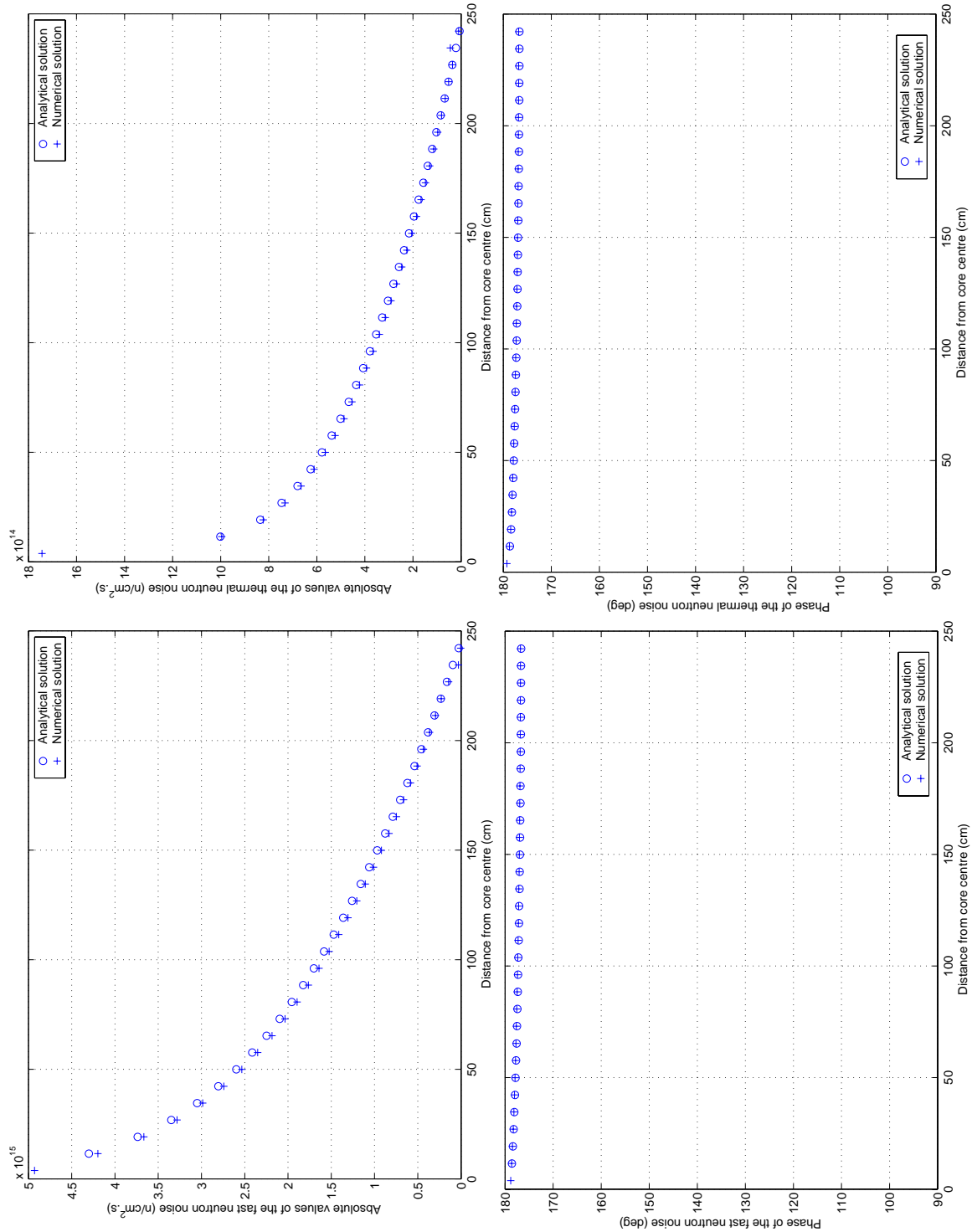


**Fig. 4.** Comparison between the analytical and numerical solutions, for the case of a thermal absorption cross-section noise source

maximum number of nodes that a 32-bit code could permit. Consequently, an acceptable level of accuracy could only be achieved if a more efficient discretization scheme than the finite difference one is used. Nodal methods or finite elements are planned to be considered in the near future at our Department.

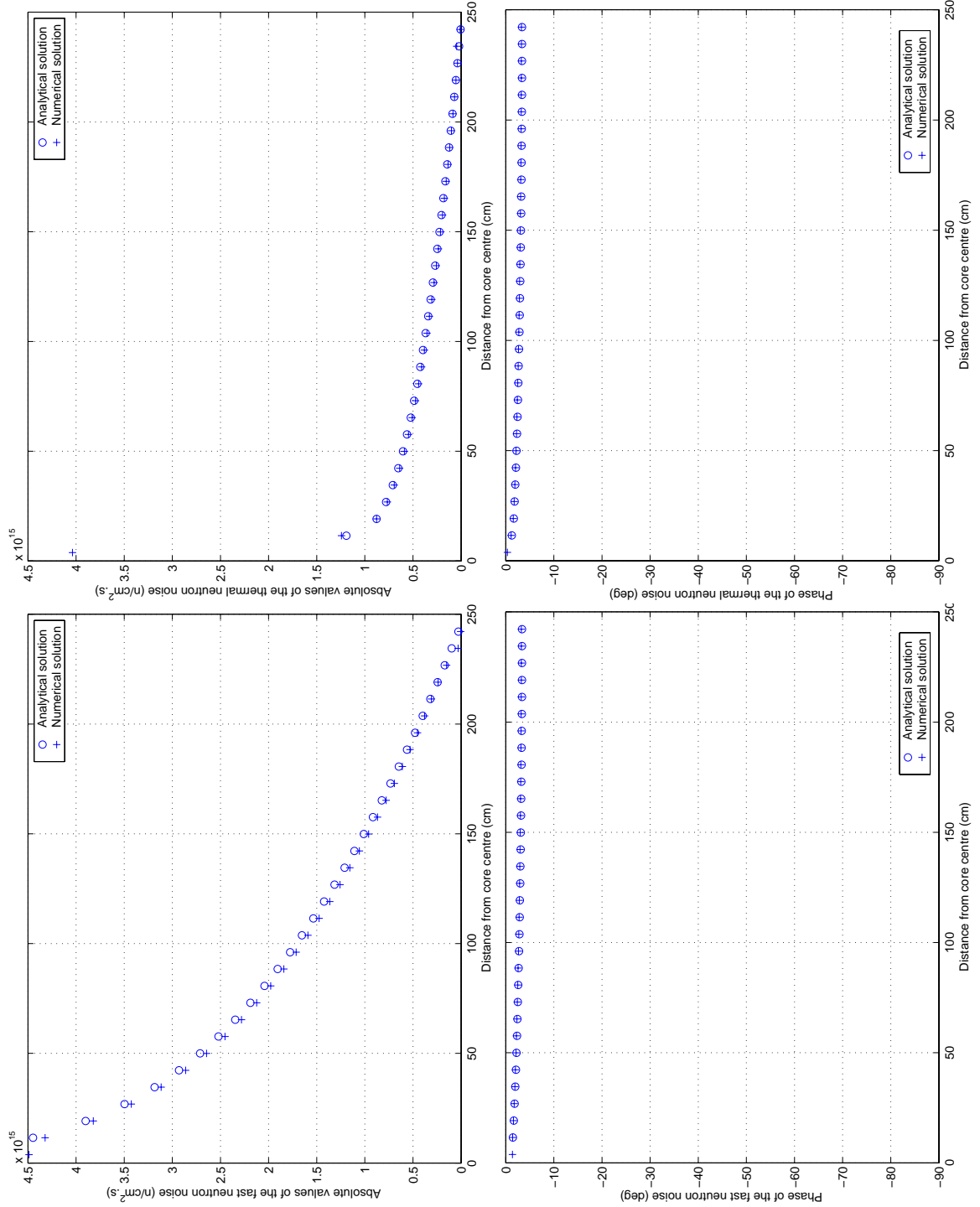


**Fig. 5.** Comparison between the analytical and numerical solutions, for the case of a removal cross-section noise source

## 1.4 Conclusions

In this Section, a 2-D 2-group neutron noise simulator, relying on the diffusion approximation, was presented. The spatial discretization scheme used is the finite difference scheme. Such a simulator was already briefly presented in stage 6, but much effort has been spent on improving the calculational efficiency since then. The noise simulator calculates the transfer function between any possible location of a noise source in

the core and the neutron noise. Due to the large size of the matrix representing the transfer function, the calculational speed is for instance quite crucial in a diagnostic task such as the localisation algorithm reported on in the next Section. The CPU time required to perform the calculation of a typical BWR core with 2x2 sub-nodes per assembly is now reasonable, which means that scanning a frequency range in order to estimate the frequency-dependent transfer function of the reactor seems to be realistic. Even if a fully coupled neutronic/thermal-hydraulic 3-D noise simulator is still interesting and will be developed at a later stage, this entirely neutronic 2-D calculator allows estimating and investigating many qualitative aspects of the neutron noise in a reactor core. Some of them have already some practical applications, such as the localisation of a noise source from the detector readings (see next Section).

Even if the benchmarking of this simulator for homogeneous cores showed that the agreement between the numerical and analytical solutions was excellent for both the amplitude and the phase of the flux noise, it is believed that the accuracy could deteriorate when strongly heterogeneous cores like BWR ones are considered. This is mainly due to the fact that a finite difference scheme was used for the spatial discretization. Therefore, it appears to be appropriate to study the possibility of using a more sophisticated scheme, such as finite elements or nodal methods, for the development of a coupled neutronic/thermal-hydraulic noise simulator. Finite elements will be given special attention since a multiphysics code, named FEMLAB, is now available at our Department.

## Section 2

### Application of the neutron noise simulator to anomaly localisation

#### 2.1 Introduction

In the preceding case, the flux noise was calculated assuming that the noise source was known (both its strength and its location). Even if being able to estimate the flux noise in a reactor is undoubtedly interesting, determining the location of an unknown noise source from the neutron detector readings is even more challenging. Such an inverting capability could be directly used for diagnostic purposes. In the following, an algorithm allowing to locate the position of a noise source (but not its strength) is presented. Several test cases are also presented, so that the validity of the algorithm can be assessed. Finally, the localisation procedure is used in a practical case, namely the Forsmark 1 local instability event.

#### 2.2 Localisation algorithm

The localisation algorithm is the one developed previously by Karlsson and Pázsit [14], [15]. Therefore, only the basic principles of this procedure are recalled in the following. More details can be found in the original papers.

If one assumes that there is only one noise source located in the node  $(I_0, J_0)$ , the flux noise can be calculated from Eq. (21). This can be written in a condensed form as follows:

$$\begin{bmatrix} \delta\phi_{1,I,J}(\omega) \\ \delta\phi_{2,I,J}(\omega) \end{bmatrix} = \overline{\overline{G}}(I_0, J_0 \rightarrow I, J; \omega) \times \begin{bmatrix} S_{1,I_0,J_0}(\omega) \\ S_{2,I_0,J_0}(\omega) \end{bmatrix} \quad (36)$$

$\overline{\overline{G}}(I_0, J_0 \rightarrow I, J; \omega)$  is in fact the discretised two-group Green's function of the system, which is evaluated by the noise simulator. Conceptually,  $\overline{\overline{G}}(I_0, J_0 \rightarrow I, J; \omega)$  is a 2x2 matrix and the multiplication in Eq. (36) is a matrix multiplication. Since neutron detectors are most often sensitive to the thermal flux, one can write also:

$$\delta\phi_{2,I,J}(\omega) = \overline{G}_2(I_0, J_0 \rightarrow I, J; \omega) \times \begin{bmatrix} S_{1,I_0,J_0}(\omega) \\ S_{2,I_0,J_0}(\omega) \end{bmatrix} \quad (37)$$

or more simply:

$$\delta\phi_{2,I,J}(\omega) = \overline{G}_2(I_0, J_0 \rightarrow I, J; \omega) \times S_{I_0, J_0}(\omega) \quad (38)$$

where  $\overline{G}_2(I_0, J_0 \rightarrow I, J; \omega)$  is the second row of the  $\overline{\overline{G}}(I_0, J_0 \rightarrow I, J; \omega)$  matrix and correspondingly the multiplication in Eqs. (37) and (38) is a scalar product.

Estimating the ratio between the flux noise measured at two different locations  $A$  and  $B$  allows eliminating the noise source strength:

$$\frac{\delta\phi_{2, I_A, J_A}(\omega)}{\delta\phi_{2, I_B, J_B}(\omega)} = \frac{\overline{G}_2(I_0, J_0 \rightarrow I_A, J_A; \omega)}{\overline{G}_2(I_0, J_0 \rightarrow I_B, J_B; \omega)} \quad (39)$$

The left-hand-side of Eq. (39) can be obtained from measurements. The right-hand-side contains the unknown of the problem, namely the location of the noise source. The transfer or Green's functions can be calculated to any combination of their argument, but the source position  $(I_0, J_0)$  is not known. It is given by the values for which Eq. (39) is fulfilled. The localisation algorithm will thus calculate the right-hand-side of Eq. (39) for all possible locations of a single noise source within the core and will retain the one giving the ratio of the detector signals, i.e. the left-hand-side of Eq. (39).

In reality the equality will not be complete due to background noise and other disturbing effects, thus some procedure utilising redundancy is used for a best estimate. If one has access to several detectors, the following quantity can be evaluated for each detector combination  $(A, B)$ :

$$\Delta_{A, B}(I, J) = \frac{\delta\phi_{2, I_A, J_A}(\omega)}{\delta\phi_{2, I_B, J_B}(\omega)} - \frac{\overline{G}_2(I, J \rightarrow I_A, J_A; \omega)}{\overline{G}_2(I, J \rightarrow I_B, J_B; \omega)} \quad (40)$$

so that the minimum of the following function should correspond to the location of the noise source  $(I_0, J_0)$ :

$$\Delta(I, J) = \sum_{A, B} \Delta_{A, B}^2(I, J) \quad (41)$$

Since it is common practice to use the Auto- and Cross-Power Spectral Densities (APSDs and CPSDs respectively) of the measured signals instead of their Fourier transform, Eqs. (40)-(41) have to be written as follows:

$$\begin{aligned} \Delta_{A, B, C, D}(I, J) & \quad (42) \\ &= \frac{CPSD(A, B, \omega)}{CPSD(C, D, \omega)} - \frac{\overline{G}_2(I, J \rightarrow I_A, J_A; \omega) \times \overline{G}_2^*(I, J \rightarrow I_B, J_B; \omega)}{\overline{G}_2(I, J \rightarrow I_C, J_C; \omega) \times \overline{G}_2^*(I, J \rightarrow I_D, J_D; \omega)} \end{aligned}$$

and

$$\Delta(I, J) = \sum_{A, B, C, D} \Delta_{A, B, C, D}^2(I, J) \quad (43)$$

Despite the apparent high number of possible detector combinations, the number of detectors quadruplets that need to be taken into account can be significantly reduced if the redundant combinations are discarded. For the sake of brevity, these simplifications are not presented here. We refer to the original paper instead [15].

### 2.3 Sensitivity of the algorithm

The localisation algorithm described previously can be easily tested since the noise simulator allows generating the flux noise for a given noise source. More precisely, one will assume a given location of a noise source within the core, and calculate the corresponding flux noise. The flux noise will then be used as detector signal input to the localisation algorithm. This procedure should return the (known) location of the noise source, if the localisation procedure is correct. The sensitivity of the localisation algorithm to different parameters can therefore be assessed. These parameters are the number of detector signals used, the position of the noise source, the possibility of having several noise sources, the contamination of the detector signal by external noise, and finally the transfer function used for the localisation.

In the following, the results will be presented in two types of Figures, one depicting the  $\Delta(I, J)$  function in a 3-D plot, and another one depicting also the  $\Delta(I, J)$  function but in a 2-D plot (core map). In this latter case, the detectors are also positioned via crosses ('X'). The white ones indicate the detectors used in the localisation, whereas the black ones the detectors which were *not* used. The noise source is marked by a white asterisk ('\*'), and the result of the localisation algorithm is denoted by a white circle ('O'). The core layout and the location of the detectors correspond to the Forsmark 1 BWR. Nevertheless, the cross-sections used in these test cases are representative of a two-region system (fuel + reflector regions), assumed to be homogeneous before the necessary adjustment of the cross-sections for criticality. More details regarding these cross-sections sets can be found in Section 2.4 "Cross-sections".

The first Figure (Fig. 6) represents the effect of using a reduced number of detectors. The peaks in the  $\Delta(I, J)$  function correspond to the detector locations. At these spots, the accuracy is better than away from the detectors. Therefore, since the noise source is not located at any of the detector positions, a local maximum of the function  $\Delta(I, J)$  is expected. As pointed out previously, although eliminating the redundant detectors combinations allows reducing significantly the calculation time, taking all the detectors into account still requires too much CPU effort. Furthermore, in most cases only a few number of detector signals are actually available from measurement campaigns. Therefore, the localisation algorithm was tested in two cases: first assuming that all the detectors were available, second by using only the four detectors surrounding the noise source. As can be seen in Fig. 6, the noise source is correctly located when using a reduced set of detectors. Even if using as many detectors as possible would seem to be the most logical choice, in the following test cases only the detectors neighbouring the noise source are used. This does not affect the success of the localisation algorithm negatively.

The right-hand-side of Fig. 6, together with Fig. 7, allows also noticing that the precision of the localisation algorithm is perfectly insensitive to the location of the noise source. A noise source located close to the core boundary is as successfully detected as a central one.

Although the localisation algorithm has been designed for locating one single noise source, it is not unlikely that more than one noise source is present in the core when actual measured signals are used. The localisation algorithm, on the other hand, is based on the assumption that there is only one noise source present. The solution, as suggested in the previous papers ([14], [15]) is that, each noise source is located from the signals of detectors that surround the source in question. This strategy works as long as the different noise sources are sufficiently separated. This assumption was tested in the simulations. As can be

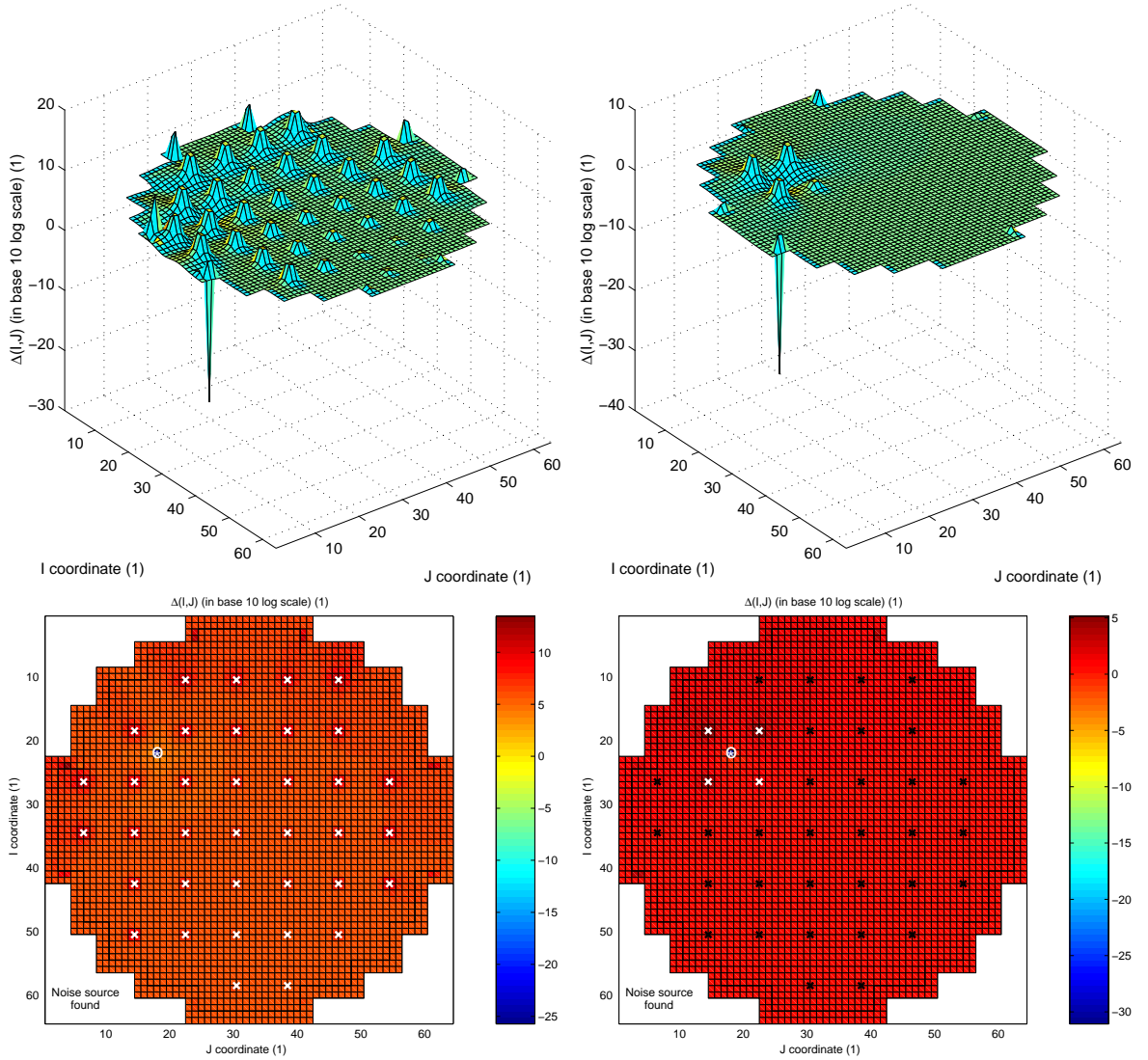


**Fig. 6.** Result of the localisation algorithm when all the detectors are used (left-hand-side) and when only the detectors surrounding the noise source are used (right-hand-side)

seen on Fig. 8, choosing a set of detectors positioned close to one of the noise sources allows detecting successfully the corresponding one, as long as the two noise sources are not too close.

The algorithm needs also to be tested when extraneous random noise is added to the detector signals before performing the noise source localisation. As can be seen in Fig. 9, the noise source is still correctly located even with as much as 10% of extraneous noise. One could notice nevertheless that the dip in the  $\Delta(I, J)$  function is less accentuated with noise than without noise (see for instance Fig. 6). The main reason that could explain why the noise source is still correctly located with a relatively high level of background noise is that in the present work, in contrast to all previous work, the noise source was assumed to be given as a perturbation of the removal cross-section. As can be seen on Figs. 3-5, the thermal flux noise decreases much more rapidly away from the source for a removal cross-section noise source than for a fast or thermal absorption cross-section noise source. Therefore, using the transfer function between the removal cross-section noise and the thermal flux noise in the localisation algorithm is expected to provide a more pronounced

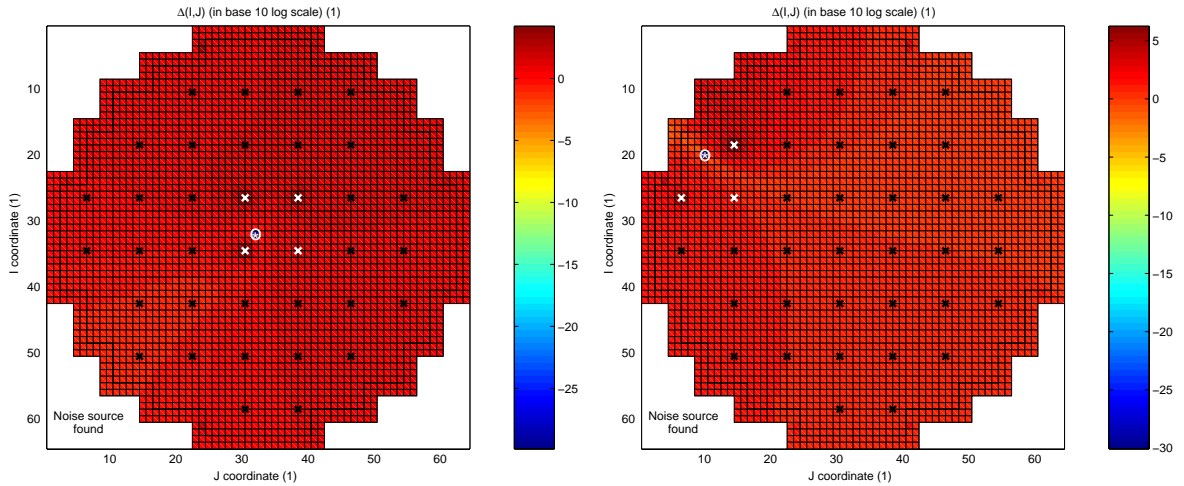


**Fig. 7.** Result of the localisation algorithm for a central noise source (left-hand-side) and a peripheral noise source (right-hand-side)

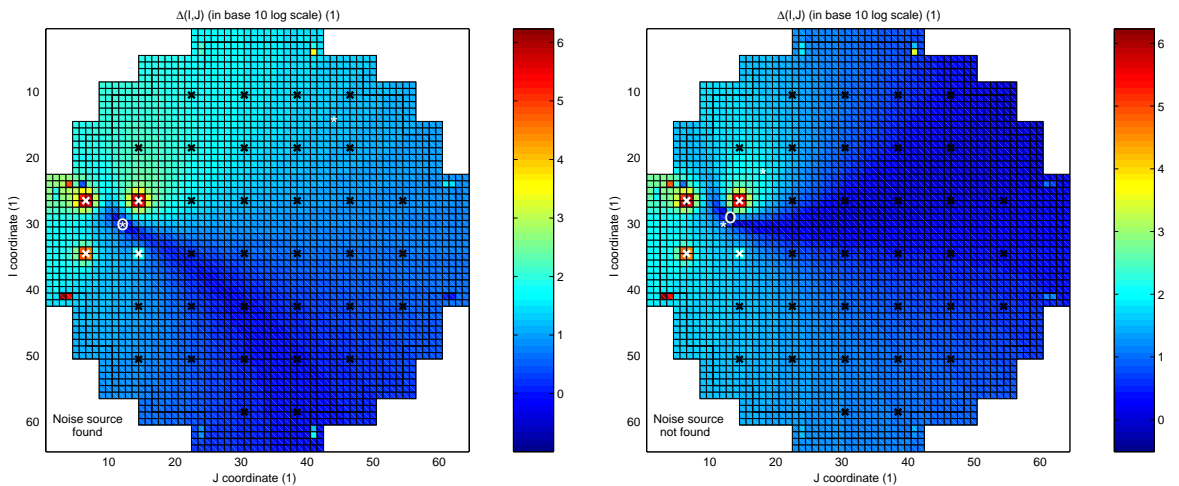


**Fig. 8.** Result of the localisation algorithm for two noise sources located far away from each other (left-hand-side) or close to each other (right-hand-side)

minimum in the  $\Delta(I, J)$  function at the location of the noise source. The use of this transfer function is consequently less sensitive to the background noise. For the sake of brevity, the 3-D plot of the  $\Delta(I, J)$  function is not depicted if one assumes that the noise source is defined in terms of the fast or thermal absorption cross-section noise, but one would have noticed that the dips corresponding to the actual noise source location are less obvious in these cases (this is particularly true for the thermal absorption cross-section case).

## 2.4 The Forsmark 1 local instability event

In 1996, during the start-up tests of the Forsmark 1 BWR for the fuel cycle 16, local instabilities were detected at reduced power and reduced core-flow. Although BWRs are known to become less stable at reduced power/core flow, the appearance of this instability event could not be understood and was not predicted by the stability calculations. The corresponding operating point in the power/flow map was therefore avoided. In January 1997, at approximately Middle Of Cycle conditions (MOC), stability measurements were carried out in order to study the local instability discovered previously. The core was thus

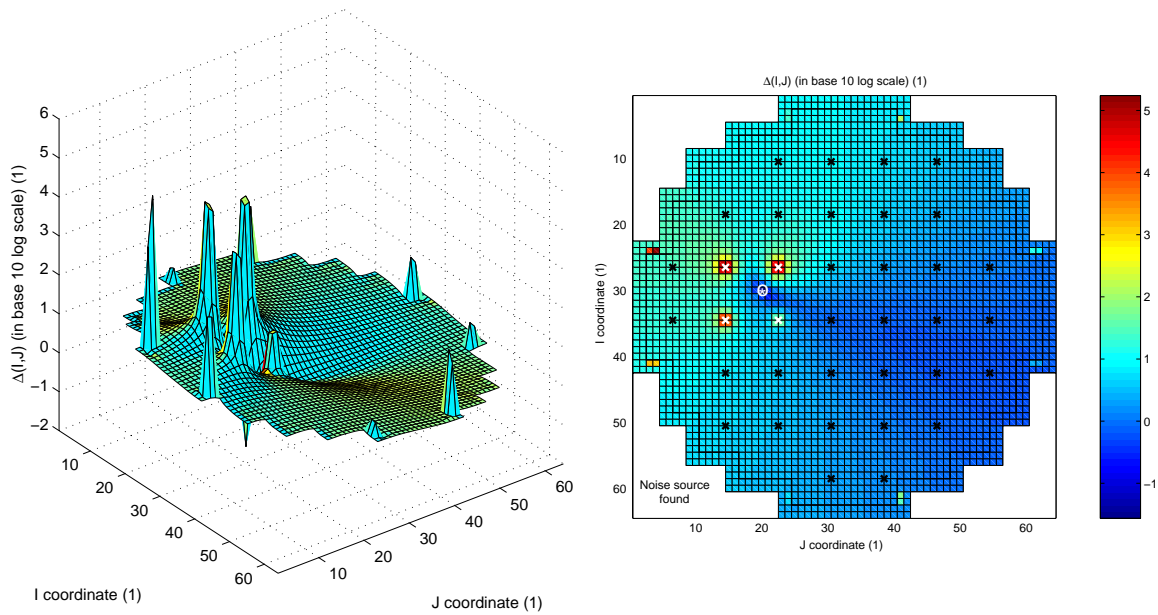


**Fig. 9.** Result of the localisation algorithm when the detector signals are contaminated by 10% of extraneous noise

brought to 63.3% of power and to a core flow of 4298kg/s. Again local instability conditions were encountered, at a frequency of roughly 0.5Hz.

During this stability measurement the lower plane of the core was rather well equipped with LPRMs (27 of the 36 available detector strings were actually recorded). A closer look at the phase of the measured flux noise indicated that the neutron noise was driven by a local noise source, similar to the effect of an absorber of variable strength (reactor oscillator), rather than a moving absorber, such as a vibrating control rod. The localisation algorithm presented previously allows locating a noise source of variable strength. By using the detectors in the lower plane, the 2-D representation of the core is expected to give the possibility of locating the noise source.

Since the localisation algorithm relies on the noise simulator presented previously in Section 1, the static data corresponding to the Forsmark 1 core are required, i.e. the material constants, the fluxes, and the point-kinetic parameters of the core. Obviously, the detector readings corresponding to the measurement campaign when the local instability was noticed are also required as input parameters to the localisation algorithm.

## Cross-sections

Unfortunately, it has not been possible to obtain so far all the necessary static data corresponding to the Forsmark 1 core when the local instability was noticed. It is planned to repeat the localisation algorithm when these are available to us. Instead the following procedure was applied to generate static data representative of a typical BWR core, whose size and core layout are the ones of the Forsmark 1 core. The cross-sections thus obtained were already used previously in the test cases of the localisation algorithm (see Section 2.3).

A model developed previously at the Department of Reactor Physics, Chalmers University of Technology was used as a starting point [16]. More specifically, this model is representative of a typical General Electric BWR/6 at EOC and equilibrium. The fuel

elements are only typical UOX BWR bundles. From this core, the cross-sections, diffusion coefficients and fluxes are obtained in the two-group formulation and for each node of the core. The point-kinetic data of the core are also retained. It has to be emphasized that all these data were obtained from the SIMULATE-3 code, which unfortunately does not provide the static fluxes in the reflector nodes [9]. Since these data are required to modify the cross-sections in order to fulfil the balance equations as pointed out previously, the CASMO-4 code was used for that purpose [7]. For typical fuel bundles, the ratios between the fluxes in the reflector node and its neighbouring fuel node was calculated. These ratios were then used to calculate the fluxes in the reflector nodes from the fluxes in the fuel nodes given by SIMULATE-3. Since a reflector node may be facing several fuel nodes, an iterative procedure was used for these estimations.

Second, the 3-D data were condensed into two sets of 0-D data: a set representative of all the fuel nodes, and a set representative of all the reflector nodes. Of course, the condensation was carried out by preserving the reaction rates, which means that the weighting functions used for averaging the data were the static fluxes:

$$XS_{g,region} = \frac{\int_{region} XS_g(\mathbf{r})\phi_g(\mathbf{r})d\mathbf{r}}{\int_{region} \phi_g(\mathbf{r})d\mathbf{r}} \quad (44)$$

with

$$\phi_{g,region} = \frac{\int_{region} \phi_g(\mathbf{r})d\mathbf{r}}{\int_{region} d\mathbf{r}} \quad (45)$$

Even if these data are now 0-D data, they are still representative of a 3-D system, whereas the data required for the noise simulator should be representative of a 2-D system. In concrete terms, the leakage in the axial direction has to be taken into account in the 2-D system as well and added to the absorption cross-sections in both groups.

Furthermore, the size of the General Electric BWR/6 core differs a little bit from the Forsmark 1 core. Therefore, it is very unlikely that the system is still critical when the system is adjusted to the size of Forsmark 1. In short, the criticality condition has to be fulfilled for the two-region system, of which the size of the core and the size of the reflector correspond to the Forsmark 1 core. The criticality condition is given by:

$$\begin{vmatrix}
J_0(\mu_c R_c) & I_0(\nu_c R_c) & -(I_0(\mu_r R_c) - \alpha K_0(\mu_r R_c)) & 0 \\
S_{\mu_c} J_0(\mu_c R_c) & S_{\nu_c} I_0(\nu_c R_c) & -S_{\mu_r} (I_0(\mu_r R_c) - \alpha K_0(\mu_r R_c)) & -(I_0(\nu_r R_c) - \beta K_0(\nu_r R_c)) \\
-D_{1,c} \mu_c J_1(\mu_c R_c) & D_{1,c} \nu_c I_1(\nu_c R_c) & -D_{1,r} \mu_r (I_1(\mu_r R_c) + \alpha K_1(\mu_r R_c)) & 0 \\
-D_{2,c} \mu_c S_{\mu_c} J_1(\mu_c R_c) & D_{2,c} \nu_c S_{\nu_c} I_1(\nu_c R_c) & -D_{2,r} \mu_r S_{\mu_r} (I_1(\mu_r R_c) + \alpha K_1(\mu_r R_c)) & -D_{2,r} \nu_r (I_1(\nu_r R_c) + \beta K_1(\nu_r R_c))
\end{vmatrix}$$

(46)

with

$$\alpha = \frac{I_0(\mu_r R_r)}{K_0(\mu_r R_r)} \quad (47)$$

$$\beta = \frac{I_0(\nu_r R_r)}{K_0(\nu_r R_r)} \quad (48)$$

$$\mu_c = \sqrt{\frac{-(\Sigma_{t,1,c} D_{2,c} + \Sigma_{a,2,c} D_{1,c}) + \sqrt{\Delta}}{2D_{1,c} D_{2,c}}} \quad (49)$$

$$\nu_c = \sqrt{\frac{\Sigma_{t,1,c} D_{2,c} + \Sigma_{a,2,c} D_{1,c} + \sqrt{\Delta}}{2D_{1,c} D_{2,c}}} \quad (50)$$

$$\mu_r = \sqrt{\frac{\Sigma_{t,1,r}}{D_{1,r}}} \quad (51)$$

$$\nu_r = \sqrt{\frac{\Sigma_{a,2,r}}{D_{2,r}}} \quad (52)$$

$$S_{\mu_c} = \frac{\Sigma_{rem,c}}{D_{2,c} \mu_c^2 + \Sigma_{a,2,c}} \quad (53)$$

$$S_{\nu_c} = \frac{\Sigma_{rem,c}}{-D_{2,c} \nu_c^2 + \Sigma_{a,2,c}} \quad (54)$$

$$S_{\mu_r} = \frac{\Sigma_{rem,r}}{\Sigma_{a,2,r} - \frac{D_{2,r}}{D_{2,r}} \Sigma_{t,1,r}} \quad (55)$$

and

$$\Sigma_{t,1,c} = \Sigma_{a,1,c} + \Sigma_{rem,c} - \frac{\nu \Sigma_{f,1,c}}{k}, \quad (56)$$

$$\Sigma_{t,1,r} = \Sigma_{a,1,r} + \Sigma_{rem,r}, \quad (57)$$

$$\Delta = (\Sigma_{t,1,c}D_{2,c} + \Sigma_{a,2,c}D_{1,c})^2 + 4D_{1,c}D_{2,c}\Sigma_{rem,c}\frac{v\Sigma_{f,2,c}}{k}. \quad (58)$$

The indices  $c$  and  $r$  stand for *core* and *reflector* respectively.  $R_c$  and  $R_r$  represent the outer radius of the fuel zone and of the reflector zone respectively. The criticality is adjusted by modifying the eigenvalue  $k$ .

From this system, the critical fluxes can be calculated according to the following equations:

$$\begin{bmatrix} \phi_{1,c}(r) \\ \phi_{2,c}(r) \end{bmatrix} = \begin{bmatrix} AJ_0(\mu_c r) + BI_0(\nu_c r) \\ AS_{\mu_c}J_0(\mu_c r) + BS_{\nu_c}I_0(\nu_c r) \end{bmatrix} \quad (59)$$

$$\begin{bmatrix} \phi_{1,r}(r) \\ \phi_{2,r}(r) \end{bmatrix} = \begin{bmatrix} C(I_0(\mu_r r) - \alpha K_0(\mu_r r)) \\ CS_{\mu_r}(I_0(\mu_r r) - \alpha K_0(\mu_r r)) + D(I_0(\nu_r r) - \beta K_0(\nu_r r)) \end{bmatrix} \quad (60)$$

with

$$A = -C \times \frac{\Re_{13}\Re_{32} - \Re_{12}\Re_{33}}{\Re_{32}\Re_{11} - \Re_{31}\Re_{12}} \quad (61)$$

$$B = -C \times \frac{\Re_{33}\Re_{11} - \Re_{31}\Re_{13}}{\Re_{32}\Re_{11} - \Re_{31}\Re_{12}} \quad (62)$$

$$D = -\frac{A\Re_{21} + B\Re_{22} + C\Re_{23}}{\Re_{24}} \quad (63)$$

where  $\Re$  represents the matrix given by Eq. (46) and the element  $(i,j)$  is given by  $\Re_{ij}$  ( $i$  row index, and  $j$  column index). Of course, the flux level was adjusted via the coefficient  $C$  so that the correct power of the reactor was achieved.

Finally, the fluxes were spatially averaged in each node by simply taking the average between the fluxes at the four corners of a node. As described previously in Section 1.2 “Data required”, the cross-sections need to be adjusted so that the balance equations are fulfilled in each node. This guarantees that the system is critical when using the finite difference discretization scheme.

### Neutron detectors readings

The localisation algorithm carries out a so-called inversion task, i.e. the noise source location is determined from the flux noise. Therefore, the neutron noise measured by the neutron detectors represents the input parameter of the localisation procedure. In the following, only the Forsmark 1 case is discussed.

In the Forsmark 1 core, 36 LPRM strings are available, and for each of them 4 different axial positions. The radial core map is depicted in Fig. 10. The different axial levels are located at 3.0912m (plane 1), 2.2080m (plane 2), 1.3616m (plane 3), and 0.5336m (plane 4) from the bottom of the core active height. Two types of measurements were performed on January 31<sup>st</sup>, 1997 during the fuel cycle 16: a measurement at 64.4% of relative power and 4416kg/s of core flow (starting time 6:39 AM), and a measurement at 63.3% of relative power and 4298kg/s of core flow (starting time 7:26 AM). The sampling frequency was 12.5Hz. Two types of signals were recorded: one measuring the LPRM signals at many radial location but for the lowermost axial level mostly (the so-called measurement type 1), and one measuring the LPRM signals at different axial locations for a few strings (the so-called measurement type 2). As usual, the Auto-Power Spectrum Densities (APSDs) of the signals have been calculated by using the Welch's averaged, modified periodogram method [17]. The mean value of each signal was first removed and then the time-signals were divided into overlapping sections of 512 points, then windowed by using a Hanning window. The sections were assumed to overlap by 256 points. Two examples of the measurement type 1 are given in Fig. 11. It is clearly seen that the second measurement, i.e. at 63.3% of relative power and 4298kg/s of core flow, reveals a peak in the APSD at a frequency of roughly 0.5Hz, which corresponds to the oscillation frequency noticed during the instability event.

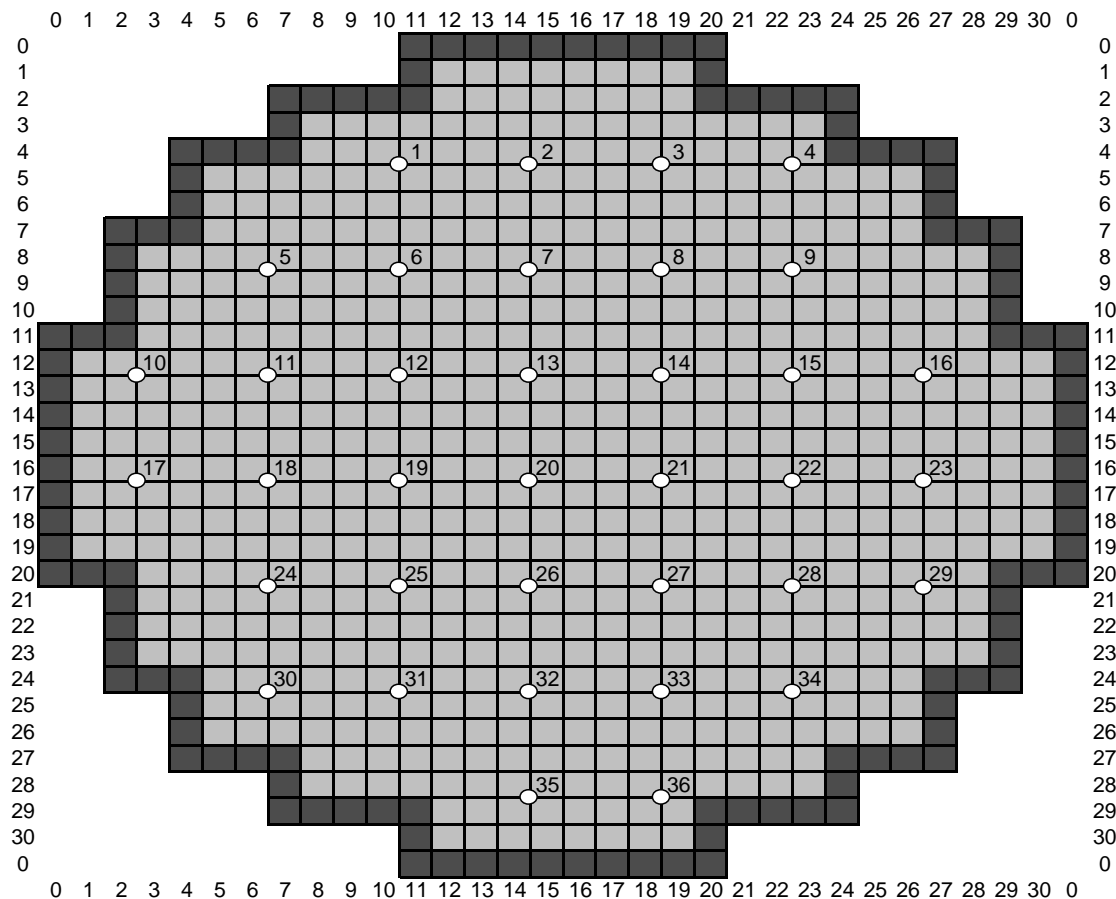


**Fig. 10.** Radial location of the LPRM strings in the Forsmark 1 reactor (the reflector nodes are dark-grey coloured)

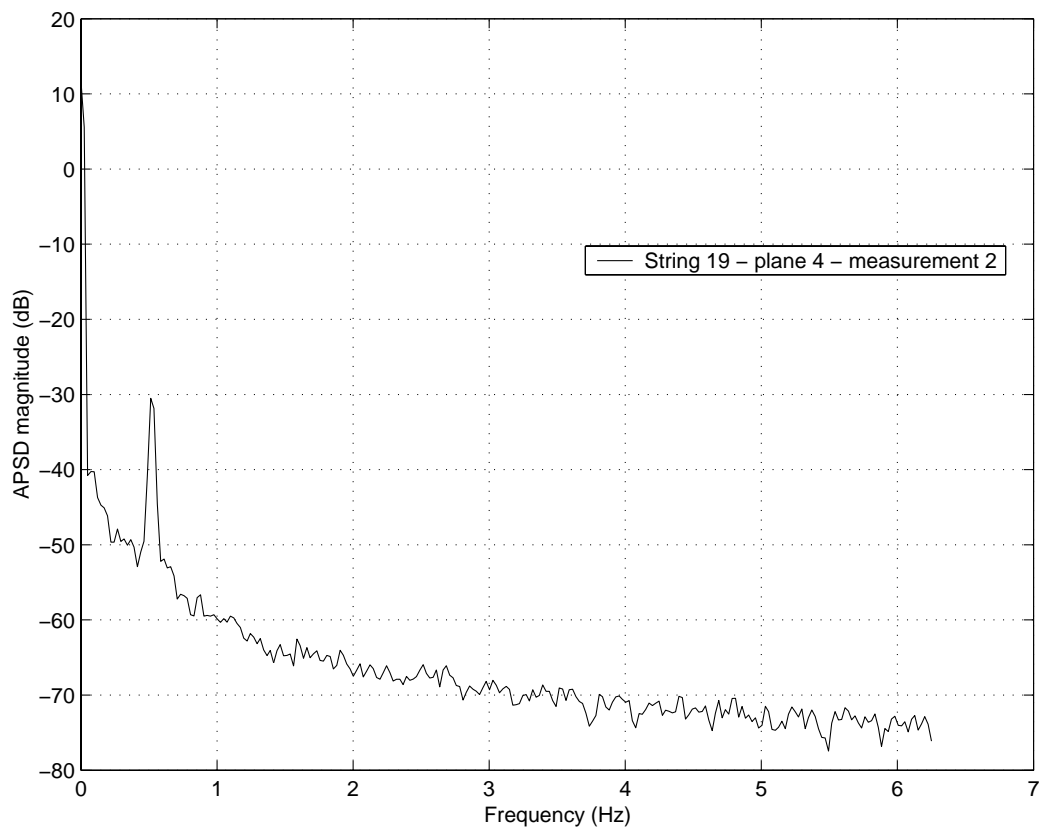
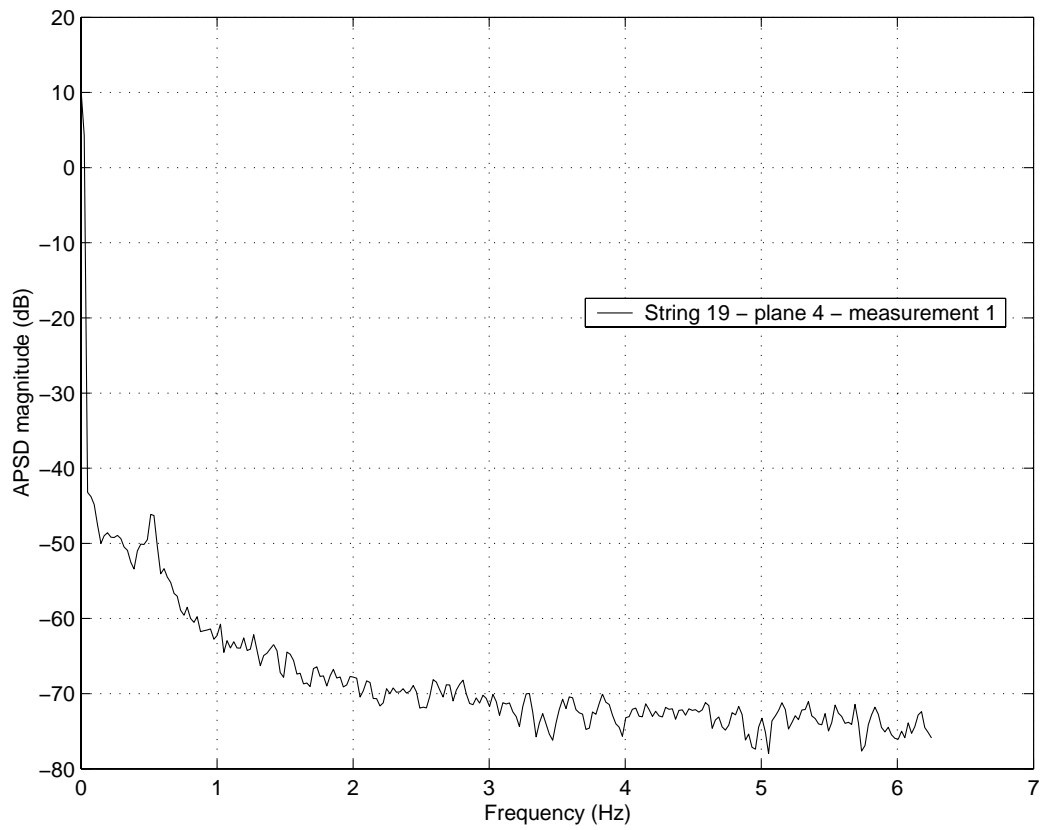


**Fig. 11.** *APSDs of the LPRM located in string 19 and plane 4 (the upper figure represents the first measurement, i.e. 64.4% of relative power and 4416kg/s of core flow, and the lower figure represents the second measurement, i.e. 63.3% of relative power and 4298kg/s of core flow)*

## Results of the localisation procedure

The results of the localisation algorithm applied to the Forsmark 1 case are presented in Fig. 12, where the transfer function between the removal cross-section noise and the thermal flux noise was used.

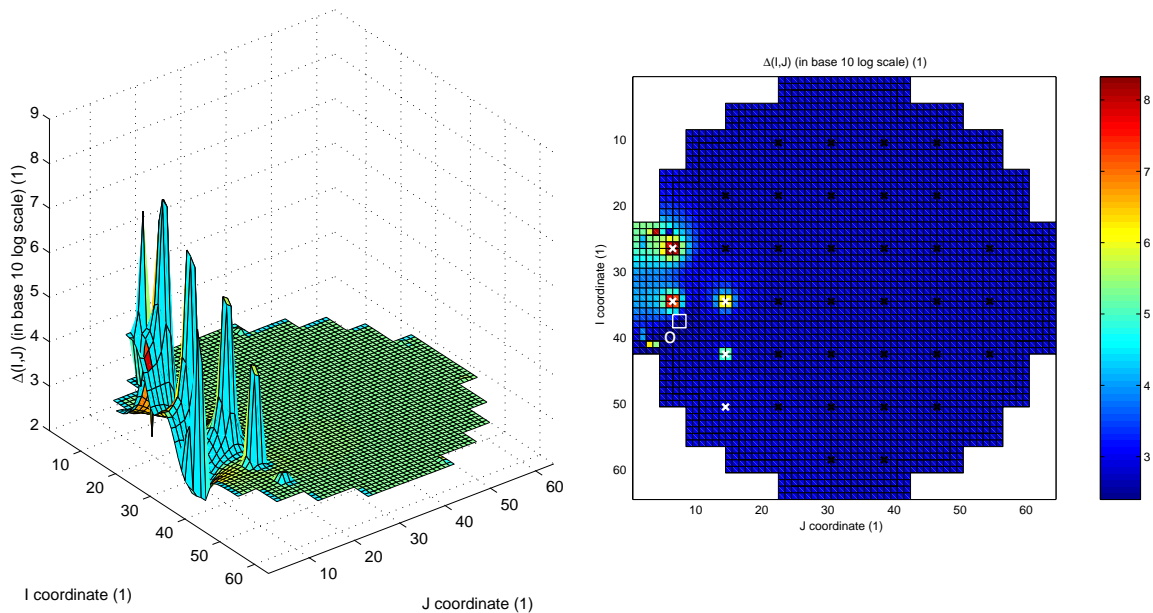


**Fig. 12.** Result of the localisation algorithm in the Forsmark 1 case (local instability event); the unseated fuel element is marked with a square, and the noise source identified by the localisation algorithm with a circle

As can be seen on Fig. 12, using a suitable set of detectors, the detectors surrounding the region where a noise source is likely to be present ([14] and [15]), the localisation algorithm gives a global minimum located in the reflector nodes. A closer examination of the  $\Delta(I, J)$  function also shows a local minimum, located in the fuel nodes. During the core outage following this instability event, a fuel assembly was found to be unseated close to the location pointed out by the localisation algorithm ([18] and [19]). Consequently, a noise source of variable strength seems to be responsible for the local instability encountered in Forsmark 1. The localised character of the noise source is in favour of a channel thermal-hydraulic instability, i.e. a self-sustained Density Wave Oscillation (DWO) [20]. As pointed out by [14] and [15], when a fuel element is unseated, some of the coolant flow bypasses the fuel element and this might render the channel thermal-hydraulically unstable.

Nevertheless choosing a different set of detectors gives results which are sometimes different, i.e. the noise source is not always located at a position close to the unseated fuel element. This suggests that there are probably two (or maybe even more) noise sources located inside the core. As pointed out previously, limiting the number of detectors to a region where a noise source is suspected to be located allows successfully locating this specific noise source, as long as the other noise sources are not in the same vicinity. This is why the region around the unseated fuel element was pointed out by the localisation algorithm. Taking more detectors into account than the one used in Fig. 12 is equivalent to take the effect of several other possible noise sources into account, whereas the algorithm has been designed for a single noise source. Finally, it is worth mentioning that only the

region pointed out by the localisation algorithm was visually inspected during the core outage, i.e. other unseated fuel elements might have remained undetected.

## 2.5 Conclusions

In this section, the noise simulator presented previously was used in an inverting task, namely the localisation of an unknown noise source. Neutron noise data were generated by the simulator, and these were used subsequently in the localisation algorithm. From the detector readings at some discrete locations of the core in a 2-D plane, the algorithm pointed out a location corresponding to the suspected noise source, of which the strength is still undetermined. The algorithm was found to be perfectly insensitive to the number of detectors used, to the location of the noise source in the core, and to the presence of extraneous noise in the detector signals. These conclusions can be held as long as one single noise source exists in the core, since the localisation procedure was designed explicitly in this case. The presence of several noise sources deteriorates the accuracy of the localisation, but as long as the noise sources are well separated in space, using a set of detectors surrounding one of the noise sources gives the correct location of this specific noise source. Furthermore, the fact that the thermal flux noise diverges close to the noise source when the noise is defined from the removal cross-section makes the localisation algorithm more robust and more efficient than in the case where the noise source is defined in terms of the fast/thermal absorption cross-section noise.

This algorithm was finally applied to a realistic case, namely the Forsmark 1 local instability event. By selecting an appropriate set of detectors on the lowermost LPRM level in the core, the localisation algorithm pointed out a global minimum in the reflector that had to be disregarded, and a local minimum located close to a fuel element that was discovered to be unseated during the core outage. The fact that using a different combination of detectors might in some cases give different results suggests that more than one noise source is responsible for the instability. Unfortunately, only 30 fuel bundles (of which one was found to be unseated) were visually inspected, i.e. some other unseated fuel bundles might not have been detected.

In the Forsmark case, a set of homogeneous cross-sections for the fuel elements and another set of homogeneous cross-sections for the reflector were used. These cross-section sets do not correspond exactly to the Forsmark 1 core. A set of cross-sections, representative of the Forsmark 1 core, is planned to be used in future work, in the next stage.

## Section 3

### Wavelet analysis of Oskarshamn 2 data for detector tube impacting

#### 3.1 Introduction

Discovering detector tube vibrations, and especially detecting impacting, has been of interest since relatively long. This subject has been also pursued at our Department ([21] - [23], [3]). There are several ways of discovering and quantifying impacting, based on the distortion of the phase between two detectors, widening of the peak/increasing of the decay ratio associated with the vibration peak, distortion of the probability distribution function (PDF), and finally wavelet analysis.

Most of the methods are not absolute, rather relative and need access to data from the same string before impacting. Widening of a peak, decreasing of the decay ratio, distortion of the PDF are all, as the terminology discloses, methods that require a comparison to the impacting-free data in order to detect impacting.

Wavelet analysis is one of the few methods, if not the only, which to a large degree is absolute or calibration-free. It is based on a suggestion of Thie [24] that each impacting of a detector tube against the wall of a fuel assembly will induce short, damped oscillations of the fuel assembly itself, which then will contribute to the detector signal. High-frequency damped oscillations of the fuel assembly will manifest themselves as spikes, and the task of detecting impacting is then reduced to the task of detecting spikes in the signal. Such a detection can be performed with wavelet analysis. Even some quantification of the severity of the impacting can be performed. Study of the performance of wavelet-based impactation detection was made by using a simple wavelet type, the so-called Haar transformation ([3], [23]). Both simulated signals and measurements taken in Barsebäck-1 were investigated with success. Nevertheless it has to be emphasised that this method is based on a hypothesis, i.e. the high-frequency vibration of the fuel assembly on impacting, which is difficult to verify experimentally.

The present study is meant to be an extension of the previous wavelet study in two ways. First, we were given access to a large number of measurement data, taken by GSE Power systems, in Oskarshamn 2 between 1991-1994, through an agreement between GSE, SKI and Chalmers. Most of the data were taken by a vibration monitoring system VIBMON [29], installed by GSE in Oskarshamn in April 1992. In most cases there is also information available on whether or not impacting occurred, and if so, with what severity, through inspection of detector tube damage during refuelling. Such a set of data is invaluable for the test of an independent method. Second, we also intend to test other wavelets than the Haar wavelet, to see if there are other types that are more effective in the detection of the impacting.

Due to the large amount of data and thus the size of the task, only the first out of these two extensions were implemented in the present stage. Namely, a thorough investigation of all signals was made but only the Haar wavelets were used. The wavelet tool kit of MATLAB was purchased and some preliminary tests of both simulations and measured signals were made, but use of more sophisticated wavelets was postponed to the next stage.

The current section presents an analysis of several measurements taken at the Oskarshamn BWR unit 2 during 1991 to 1994. Table IV specifies some general information about the measurements.

**Table IV.** General information about experimental measurements

Index	Date	Time	Cycle	Power [%]	Flow [ton/s]	File name
m = 1	91-Oct-21	14:12	17	N/A	N/A	o2vib9110211412.mat
m = 2	91-Dec-09	00:00	17	105.9	5.18	o2vib9112090000.mat
m = 3	92-Apr-07	09:39	17	106.2	6.08	o2vib9204070939.mat
m = 4	92-May-06	14:58	17	106.7	7.17	o2vib9205061458.mat
m = 5	92-May-18	14:25	17	99.6	5.80	o2vib9205181425.mat
m = 6	92-May-26	13:48	17	72.5	3.16	o2vib9205261348.mat
m = 7	92-Jun-03	16:35	17	104.0	7.58	o2vib9206031635.mat
m = 8	92-Jun-16	12:01	17	100.3	7.27	o2vib9206161201.mat
m = 9	92-Jul-29	12:49	17	89.1	7.62	o2vib9207291249.mat
m = 10	93-Mar-19	09:23	18	89.1	7.62	o2vib9303190923.mat
m = 11	93-Nov-01	09:18	19	98.5	6.98	o2vib9311010918.mat
m = 12	93-Nov-18	15:36	19	100.0	5.25	o2vib9311181536.mat
m = 13	94-Jan-28	08:50	19	104.3	5.23	o2vib9401280850.mat
m = 14	94-Mar-17	14:50	19	104.4	5.67	o2vib9403171450.mat
m = 15	94-Aug-09	13:26	20	89.7	4.08	o2vib9408091326.mat
m = 16	94-Nov-29	09:15	20	104.4	5.28	o2vib9411290915.mat

### 3.2 Mathematical model

Detector string vibrations are induced by the turbulent flow of the coolant. If the vibration is strong enough, the string can eventually hit one or more fuel assemblies surrounding the detector tube. The situation is illustrated in Fig. 13.

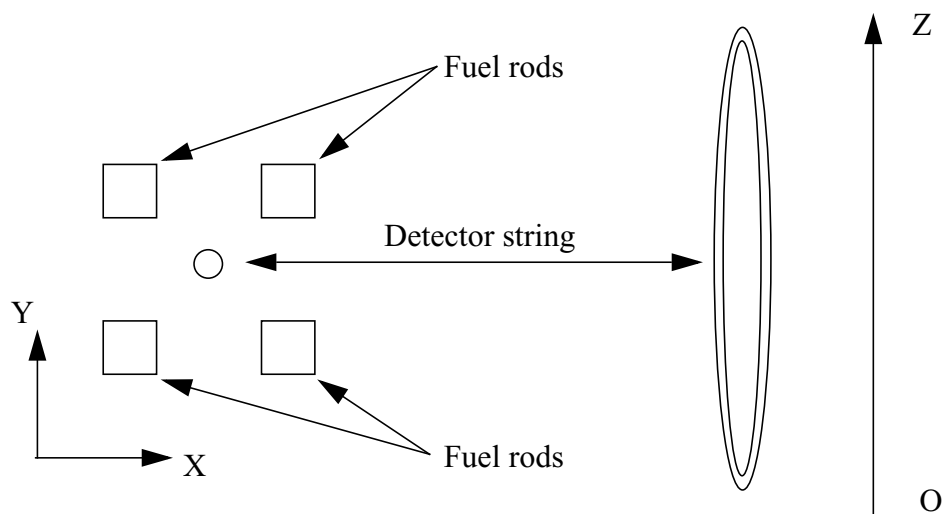


**Fig. 13.** Detector string and fuel rods

Although the vibration in the X-Y plane is two dimensional, no qualitative difference was found between 1-D and 2-D simulations [23]. Because of this fact, a simplified one dimensional simulation has been used in the current work to study the possibility to detect impacting of a detector string against surrounding fuels boxes, as shown in Fig. 14.

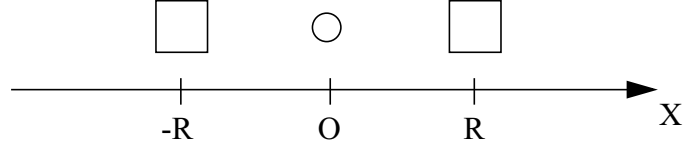


**Fig. 14.** 1-D model

Following [25], we assume that the damped oscillations of a detector guide tube may be described by the equation

$$\ddot{x}(t) + 2\theta\dot{x}(t) + \omega_0^2x(t) = f(t) \quad (64)$$

with  $\langle x(t) \rangle = 0$  being the equilibrium position,  $\theta$  standing for the damping factor and  $f(t)$  being a random driving force. It was found reasonable [25], [21] to model the stochastic force  $f(t)$  by a discrete series of impulses arriving at regular times  $t_n = n \cdot \Delta t$

$$f(t) = F_c \sum_{n=-\infty}^{n=\infty} r_n \delta(t - t_n) \quad (65)$$

where  $r_n$  is a normal random variable with mean = 0 and standard deviation = 1. The parameter  $F_c$ , also called the “force coefficient”, describes the strength of the driving force. The pulse repetition frequency must be chosen much higher than that of the oscillator, i.e.

$$\frac{1}{\Delta t} \gg \frac{\omega_0}{2\pi} \quad (66)$$

Impacting is simulated by confining the detector string motion within  $(-R, +R)$ . Whenever  $|x(t)|$ , in the course of simulation, exceeds  $R$ , the velocity  $\dot{x}(t)$  is reversed, i.e.  $\dot{x}(t) \rightarrow -\dot{x}(t)$ , which models elastic reflection from an infinite mass without energy loss. Also we assume that the neutron noise is linearly related to the mechanical vibration, i.e.

$$\delta\phi(t) = a \cdot x(t) \quad (67)$$

The model used in the current work also involves the fuel box vibration that obeys the equation

$$\ddot{X}(t) + 2\Theta\dot{X}(t) + \Omega_0^2X(t) = F(t) \quad (68)$$

where the force  $F(t)$  is induced by impactings. At each impact, the detector tube transfers a certain impulse,  $2m|\dot{x}|$ , to the fuel rod. Thus if the box/tube mass ratio is  $M/m = k$ , then, at impacting, one has  $|\dot{X}| = 2|\dot{x}|/(k + 1)$ . This will lead to the representation

$$F(t_n) = 2 \frac{M}{k+1} \cdot \delta(t-t_n) |\dot{x}(t_n)| \equiv c \cdot \delta(t-t_n) |\dot{x}_n| \quad (69)$$

Finally we assume a linear relationship between the displacement of a fuel box and the induced noise. Thus the neutron noise from a vibrating and impacting detector will be given as

$$\delta\phi(t) = a \cdot x(t) + A \cdot X(t) \quad (70)$$

### 3.3 Some theoretical tools to detect impacting

According to the model, presented briefly above, the neutron noise,  $\delta\phi(t)$ , consists of a stationary process  $a \cdot x(t)$  which is disturbed by a non-stationary process  $A \cdot X(t)$  on impacting. Wavelet analysis, as opposed to Fourier decomposition, has reportedly proved to be a powerful tool in dealing with non-stationary data [26]. Very briefly wavelet analysis consists of breaking up a signal into shifted and scaled versions of the original (mother) wavelet. More specifically, a signal  $S$  is cast into a double series

$$S(t) = \sum_{n,j} s_{n,j} \psi_{n,j}(t) \quad (71)$$

where the wavelet basis  $\psi_{j,n}(t)$  is constructed by using solely the original function  $\psi(t)$

$$\psi_{n,j}(t) = \frac{1}{\sqrt{2^j}} \psi\left(\frac{t-2^j n}{2^j}\right) \quad (72)$$

One often speaks of approximations and details. The approximations are the high-scale, low-frequency components of the signal. The details are the low-scale, high-frequency components. At the most basic level, this looks as follows:

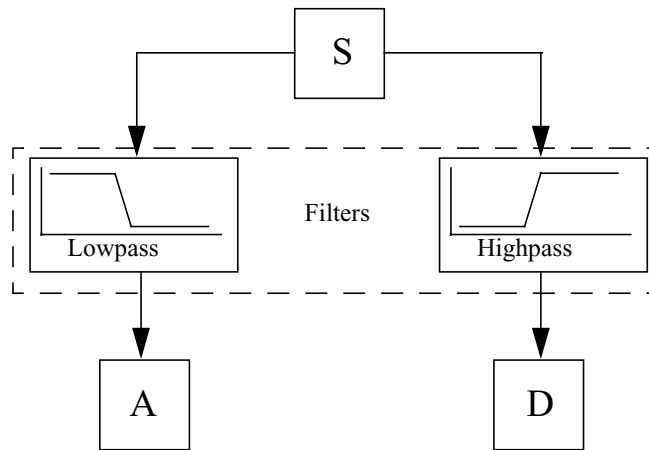


**Fig. 15.** *Approximations and Details*

Symbolically this decomposition can be written as  $S(t) = A(t) + D(t)$ . A very simple and crude, but sometimes very efficient de-noising method consists of neglecting details completely by setting  $D(t) = 0$ . A more advanced method is to set a threshold  $\tau$  and disregard all details that exceed this barrier by setting  $D(t)$  to zero

$$\hat{D}(t) = \begin{cases} D(t), & |D(t)| > \tau \\ 0, & |D(t)| \leq \tau \end{cases} \Rightarrow \hat{S}(t) = A(t) + \hat{D}(t) \quad (73)$$

In general, wavelet analysis gives a more flexible way of de-noising the signal by recursively repeating the basic decomposition into approximations and details as shown in Fig. 16.

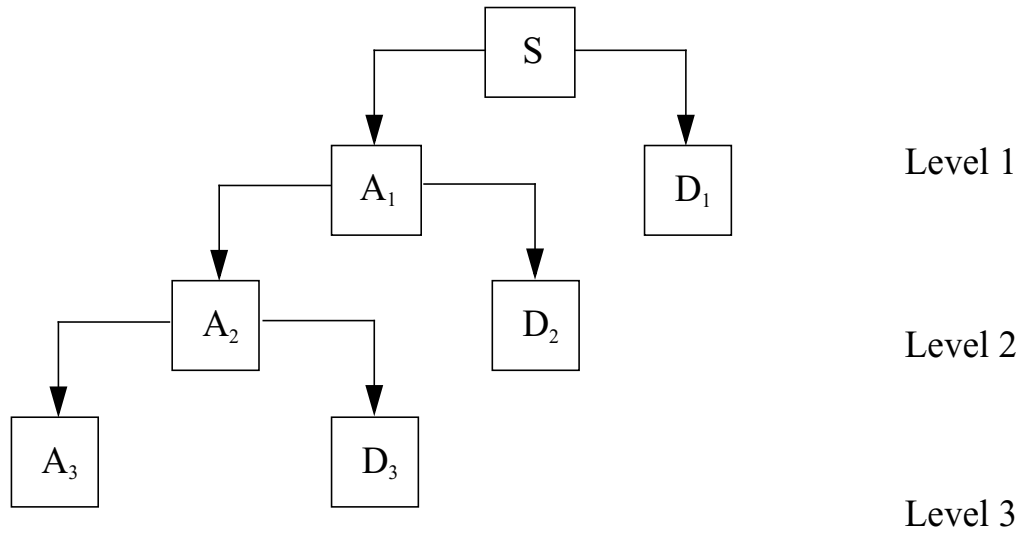


**Fig. 16.** Multi-level decomposition

The most general technique to filter the signal is to set different thresholds at different levels and afterwards to reconstruct the signal as

$$\hat{S} = A_3 + \hat{D}_3 + \hat{D}_2 + \hat{D}_1 \quad (74)$$

where a three-level decomposition has been taken as an example.

Many waveforms have been proposed as wavelets. Some examples are given in Fig. 17

The simplest wavelet analysis is based on the discrete Haar transformation which corresponds to only one level of decomposition and which can also be defined through an  $N \times N$  Haar matrix  $W$  as follows:

$$W_N = \begin{bmatrix} w_0(0) & w_0(1) & \dots & w_0(N-1) \\ w_1(0) & w_1(1) & & w_1(N-1) \\ & & & \\ & & & \\ w_{N-1}(0) & w_{N-1}(1) & \dots & w_{N-1}(N-1) \end{bmatrix} \quad (75)$$

where the entries are defined as

$$k = 1, 2, \dots, N-1 \quad m = 0, 1, \dots, \log_2(N-1) \quad n = 1, 2, \dots, 2^m$$

$$w_0(i) = 1 \quad i = 0, 1, \dots, N-1$$

$$w_k(i) = w_{2^m + n - 1}(i) = \begin{cases} 0 & i = 0, 1, \dots, 2^{-m}N(n-1) - 1 \\ +2^{m/2} & i = 2^{-m}N(n-1), \dots, 2^{-m}N\left(n - \frac{1}{2}\right) - 1 \\ -2^{m/2} & i = 2^{-m}N\left(n - \frac{1}{2}\right), \dots, 2^{-m}Nn - 1 \\ 0 & i = 2^{-m}Nn, \dots, N - 1 \end{cases} \quad (76)$$

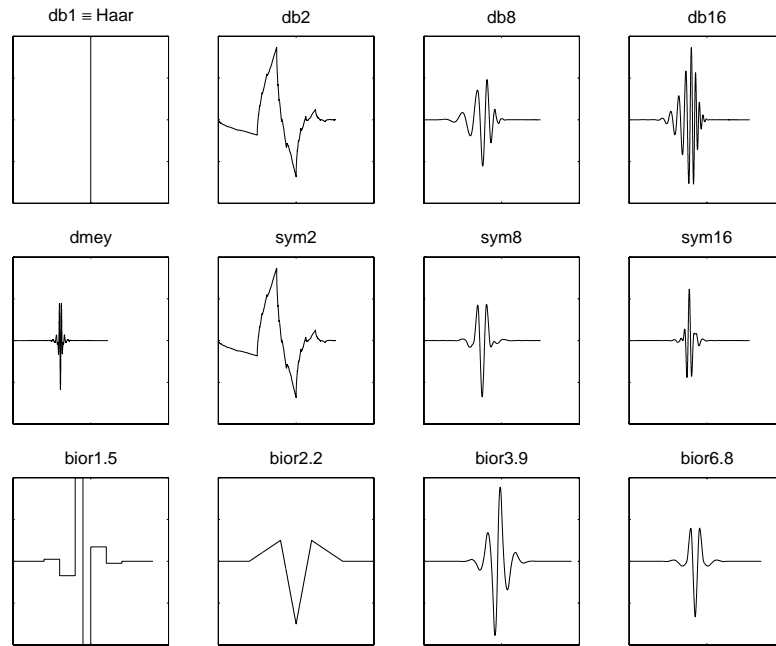


**Fig. 17.** Some wavelet examples

Now everything is ready to describe the Haar de-noising procedure of a time series  $x = \{x_0, x_1, \dots, x_{N-1}\}$  which performs the de-noising of the signal by

- applying the Haar transform  $y = W \cdot x$ ;
- thresholding  $y_k^\tau = \begin{cases} y_k & |y_k^\tau| \geq \tau \\ 0 & |y_k^\tau| < \tau \end{cases}$ ;
- applying the inverse Haar transform  $x^\tau = W^{-1} \cdot y^\tau$  to yield the amplitude filtered signal.

By a proper choice of the threshold  $\tau$  one can remove noisy (stationary) part of the original signal, whereas the transients will survive. In [23], it was found suitable to use a threshold

$$\tau = 4\sqrt{N}\sigma \quad (77)$$

which cancels almost all noise if  $\sigma$  is set to the standard deviation of the noise that is present in the signal. Determination of this standard deviation is not so easy in general and usually it requires utilizing some additional knowledge of the processes involved. In our case we assume that the signal  $x(t)$  consists of stationary ( $S$ ), transient ( $T$ ) and noisy ( $N$ ) components

as shown below

$$x(t) = S(t) + T(t) + N(t) \quad (78)$$

As known, the spectra of the stationary and transient parts have peaks about mechanical eigenfrequencies  $f_0 = \omega_0/2\pi$  and  $F_0 = \Omega_0/2\pi$ . With this information one can estimate the parameter  $\sigma$  by applying a high pass (HP) filter that leaves only a high frequency component where the noise component dominates. To this end one chooses a cut-off frequency  $f_{HP} > \max(f_0, F_0)$

$$x_{HP} \equiv HP\{x\} = HP\{S + T + N\} = HP\{S + T\} + HP\{N\} \approx HP\{N\} \quad (79)$$

Thus the standard deviation  $\sigma$  can be estimated by

$$\sigma_N^2 \approx Var[x_{HP}] \quad (80)$$

This is the principle of the method that was also used in the present analysis.

### 3.4 Numerical results with simulated data

The simulation has been performed with the following parameters:

- $\theta = 2$  - damping factor for detector string;
- $f_0 = 3.6$  - eigenfrequency of detector string;
- $\Theta = 2$  - damping factor for fuel box;
- $F_0 = 10$  - eigenfrequency of fuel box;
- $F = 4$  - driving force strength;
- $1/\Delta t = 240$  - pulse repetition frequency;
- $a = 1$  - amplitude factor for detector string vibration;
- $A = 1$  - amplitude factor for fuel box vibration;
- $R = 1$  - confinement.

Three simulated signals are shown in Fig. 18. The first one,  $a \cdot x(t)$ , comes from the detector tube, the second signal,  $A \cdot X(t)$ , is induced by the fuel box, and finally, the third plot displays the total detector signal,  $\delta\phi(t) = a \cdot x(t) + A \cdot X(t)$ . It should be noted here that the amplitude of the fuel box signal,  $A \cdot X(t)$ , is at least 1000 times weaker as compared to the detector tube signal,  $a \cdot x(t)$ , and thus it is completely invisible in the total signal,  $\delta\phi(t)$ .

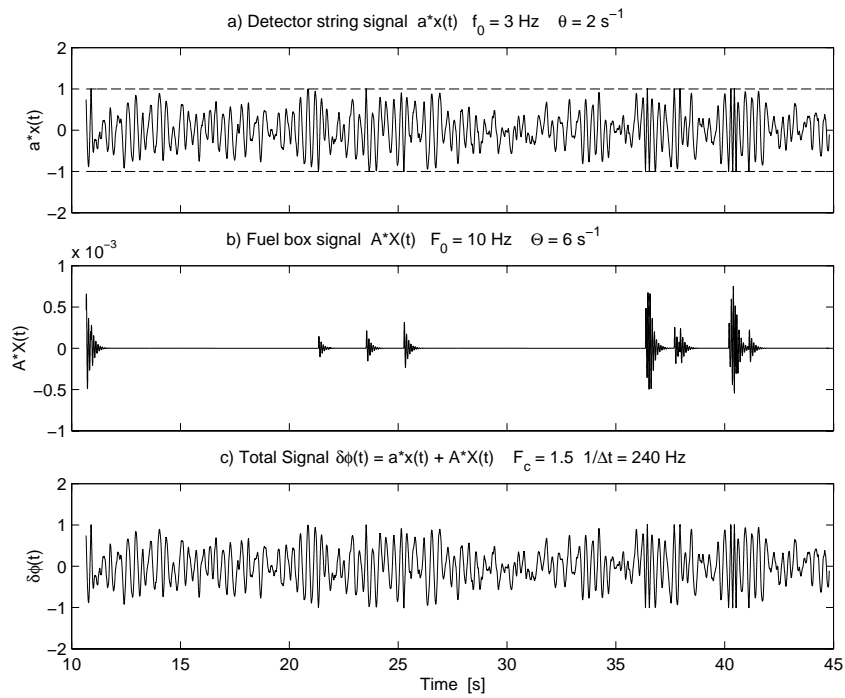


**Fig. 18.** Simulated signals

Ordinary spectral analysis cannot reveal random impact events as it is clearly seen in Fig. 19 that shows the Auto-Power Spectral Density (APSD) plot of the detector signal  $\delta\phi(t)$ . The plot shows no sign of impacting.

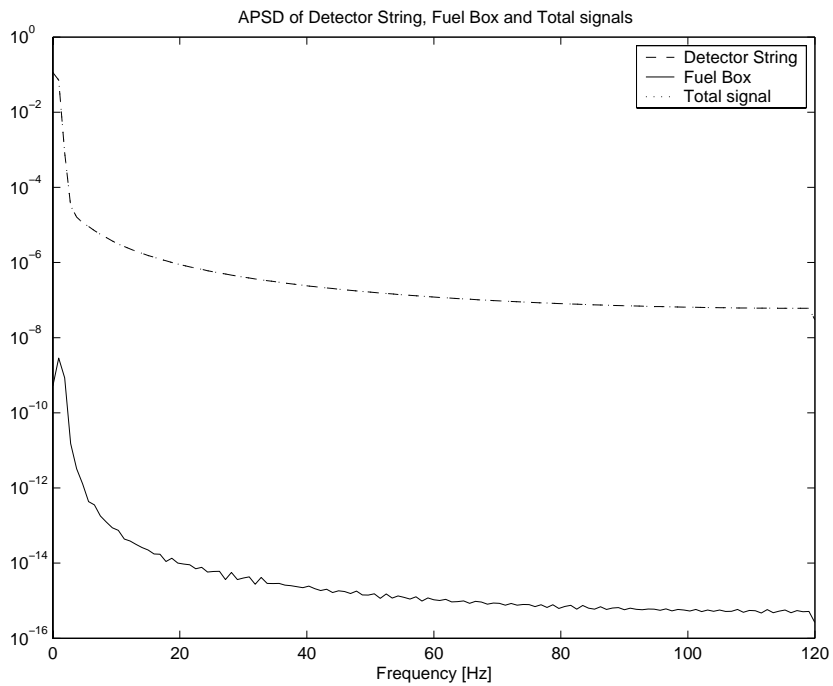


**Fig. 19.** APSD function of the signals involved

High pass filtering is illustrated in Fig. 20 that clearly reproduces every impact event.

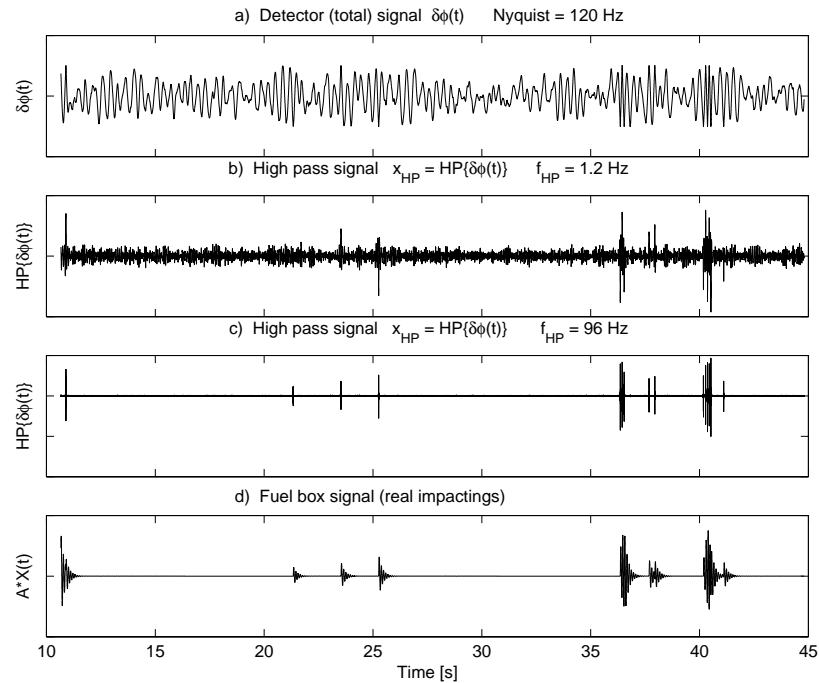


**Fig. 20.** High-pass filtering of detector signal

One can draw a simple conclusion: the higher high-pass frequency  $f_{HP}$  the better the non-stationary component is extracted from the signal.

### 3.5 Verification of detector signals

It is common practice to check the quality of signals before signal processing. Some detectors may be damaged or electronic circuits may malfunction. Sometimes one can identify this kind of situation simply by visual inspection of the signal as shown in Fig. 21.

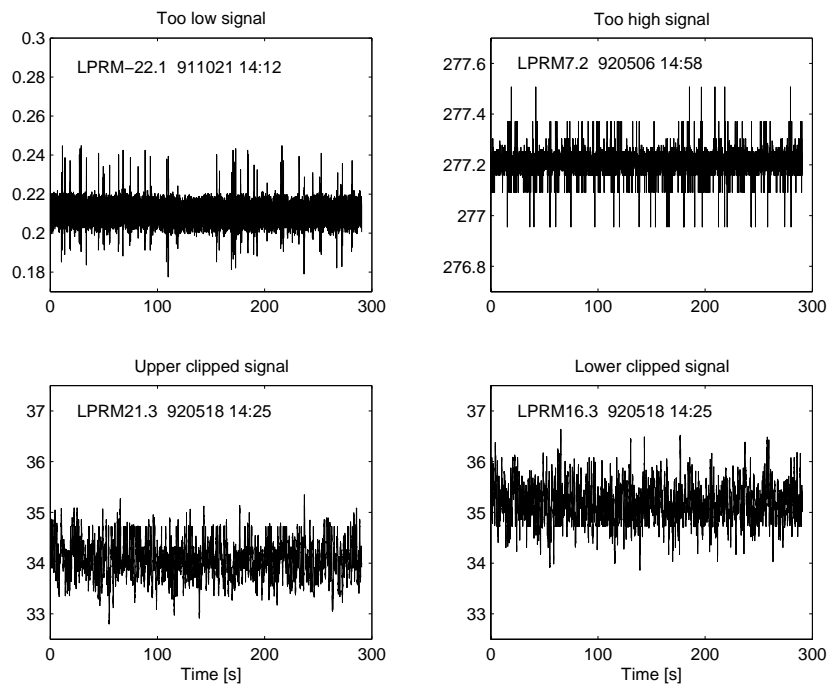


**Fig. 21.** Examples of apparently corrupt signals

In order to detect such signals automatically, several tests have been proposed.

### Low-High test

This test is based on a simple observation that a typical signal is of the order of  $50 \pm 3$  Volts. That is why the signal  $S$  having too low,  $mean(S) < 15$ , or too high,  $mean(S) > 150$  or too high standard deviation,  $std(S) > 5$ , is considered and marked as *BAD*.

### Mean value test

The mean value (MV) test utilizes the fact that typically the signal coming from the upper position, which is marked as number 1, is lower than the signal coming from the lower position, which is marked as number 2. If this is not true, i.e.  $mean(S1) > mean(S2)$ , then these signals are marked as *MV* provided both signals are available.

### Outlier test

The outlier test (*Out*) test checks if there are any sample values  $S_i$  in signal  $S$  lying by more than 4 standard deviations away from the mean value

$$\mu \equiv E[S] \quad \sigma \equiv E[(S - \mu)^2]; \quad |S_i - \mu| > 4\sigma \quad (81)$$

Only a few signals were found to have outliers. Two of them are shown in Fig. 22.

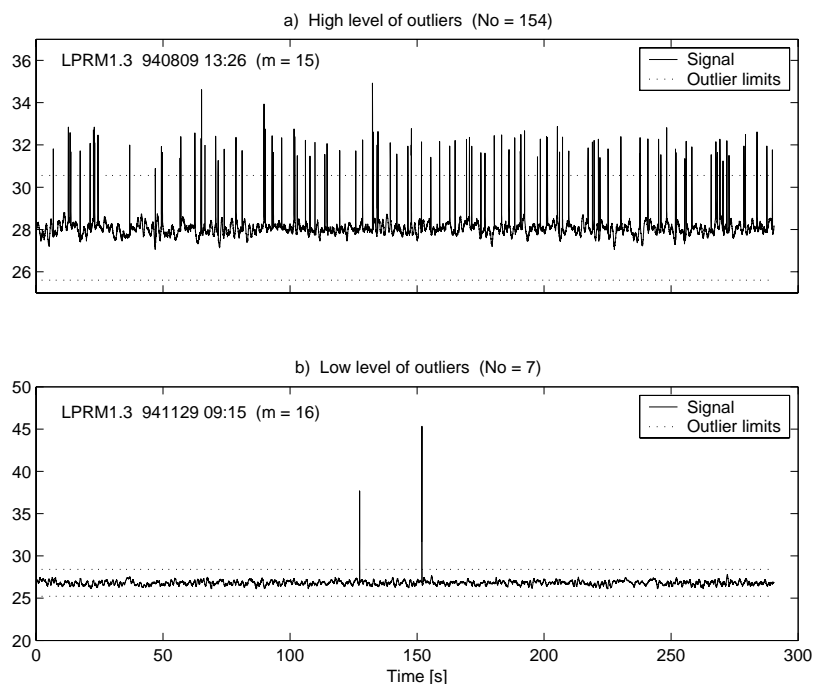


*Fig. 22. Outliers examples*

### Zero-Counts, Low-Counts and High-Counts test

This test selects the signals with unusually high or unusually low or even zero values in the corresponding histograms. More specifically, a time series of  $N$  sample  $S_i$  is sorted into  $M = \lfloor \sqrt{N} \rfloor$  equally spaced bins  $B_i$  as shown in Fig. 23.

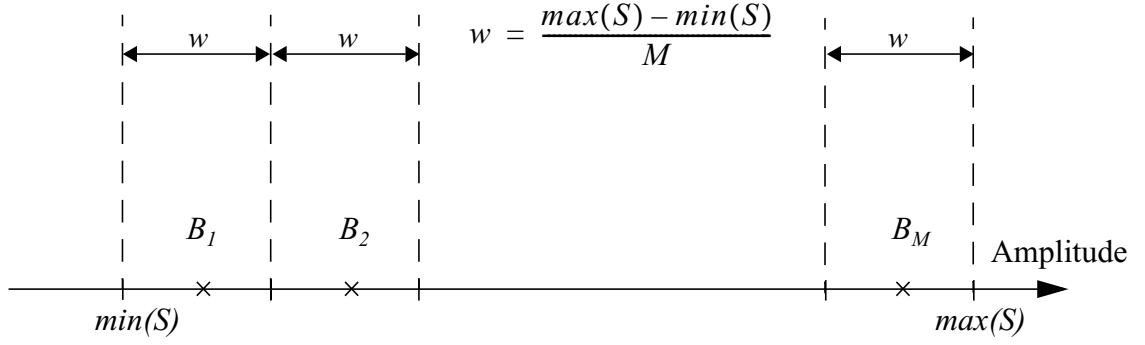


**Fig. 23.** Bin structure to plot and calculate a histogram

Then mean value  $\mu$  and standard deviation  $\sigma$  are evaluated in a usual way. Typical values are as follows:

- $N = 14528$  (number of samples);
- $M = 121$  (number of bins);
- $r = \max(S) - \min(S) \sim 10$  (range of signal);
- $w = r/M \sim 0.8$ ;
- $p = 125 \cdot 2^{-16}$  (A/D convertor precision);
- $w/p \sim 43$  (number of distinct detector values within one bin).

Because  $N$  is hopefully big, we assume a normal distribution of the counts as

$$p(x) = \frac{1}{\sigma \sqrt{2\pi}} e^{-\frac{(x-\mu)^2}{2\sigma^2}} \quad (82)$$

The next step is to select the bins with a high expected number of counts

$$\text{select } B_i \text{ such that } N \cdot p(B_i) \cdot w > 50 \quad (83)$$

Finally, the quantity  $q_i$ , which is the ratio of the actual number to the expected number of counts, is calculated for every bin satisfying (83). If  $\min(q_i) = 0$ , the signal is marked as having zero counts (ZC); if  $\min(q_i) < 1/4$ , the signal is marked as having low counts (LC), and if  $\max(q_i) > 4$ , the signal is marked as having high counts (HC). Some typical examples are presented in Fig. 24.

It should be noted here that sometimes one may guess a signal to be corrupt simply by visual inspection, as is shown in Fig. 24 b). More often it is not so visible as is seen in Fig. 24 a).

Table V summarizes results of the verification of the detector signals for all measurements. Each LPRM signal is marked as:

- B if it does not pass Low-High test;
- ? if it does pass Low-High test but fails Out, or ZC, or LC, or HC, or MV tests;
- + otherwise (it passes all tests).

Empty spot indicates that the signal is not available (N/A).

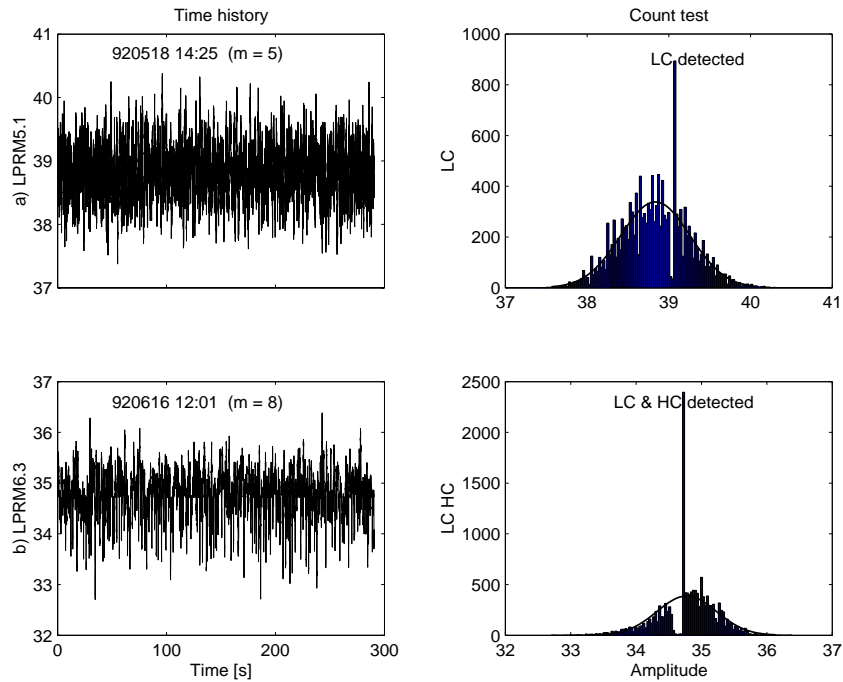


**Fig. 24.** Examples of signals with low and high counts

**Table V.** Distribution of good (+), bad (B), and questionable (?) signals.

LPRM=	1	2	3	4	5	6	7	8	9	0	1	2	3	4	5	6	7	8	9	0	1	2	3	4
Pos=	1	2	1	2	1	2	1	2	1	2	1	2	1	2	1	2	1	2	1	2	1	2	1	2
m= 1	+	+	+	+	+	+	+	+	+	+	B	?	?	+	+	+	+	+	+	+	+	+	+	+
m= 2	+	+	+	+	+	+	+	+	+	+	+	+	+	+	+	+	+	+	+	+	+	+	+	+
m= 3	?	?	?	?	?	?	?	?	?	?	?	?	?	?	?	?	?	?	?	?	?	?	?	?
m= 4	?	?	?	?	?	?	?	?	?	?	?	?	?	?	?	?	?	?	?	?	?	?	?	?
m= 5	?	?	?	?	?	?	?	?	?	?	?	?	?	?	?	?	?	?	?	?	?	?	?	?
m= 6	?	?	?	?	?	?	?	?	?	?	?	?	?	?	?	?	?	?	?	?	?	?	?	?
m= 7	?	?	?	?	?	?	?	?	?	?	?	?	?	?	?	?	?	?	?	?	?	?	?	?
m= 8	?	?	?	?	?	?	?	?	?	?	?	?	?	?	?	?	?	?	?	?	?	?	?	?
m= 9	?	?	?	?	?	?	?	?	?	?	?	?	?	?	?	?	?	?	?	?	?	?	?	?
m=10	?	?	?	?	?	?	?	?	?	?	?	?	?	?	?	?	?	?	?	?	?	?	?	?
m=11	?	?	?	?	?	?	?	?	?	?	?	?	?	?	?	?	?	?	?	?	?	?	?	?
m=12	?	?	?	?	?	?	?	?	?	?	?	?	?	?	?	?	?	?	?	?	?	?	?	?
m=13	B	B	+	?	B	B	+	+	?	?	B	+	?	?	?	?	?	?	?	?	?	?	?	?
m=14	?	?	?	?	?	?	?	?	?	?	?	?	?	?	?	?	?	?	?	?	?	?	?	?
m=15	+	?	?	?	?	?	?	?	?	?	?	?	?	?	?	?	?	?	?	?	?	?	?	?
m=16	?	?	?	?	?	?	?	?	?	?	?	?	?	?	?	?	?	?	?	?	?	?	?	?
LPRM=	1	2	3	4	5	6	7	8	9	0	1	2	3	4	5	6	7	8	9	0	1	2	3	4

The results are also presented visually in Fig. 25 to show the percentage of the LPRM signals sorted by the verification test.

A closer inspection of Fig. 25 yields several warnings that can be summarized as follows:

- the quality of detector signals worsened significantly for measurements from  $m = 3$  to 16 in contrast to measurements 1 and 2. However, measurements 1 and 2 were taken with a different data acquisition system that measurements 3 -16, which could contribute to the difference in data quality;
- the percentage of signals whose quality one may question is more than 50% on the average, sometimes reaching a level of about 75% ( $m=11$ ).

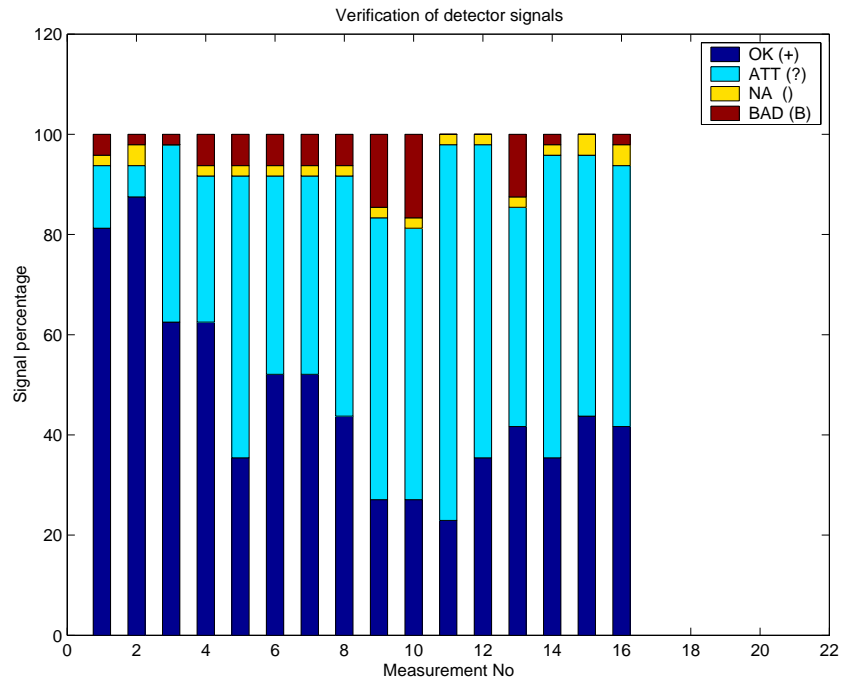


**Fig. 25.** Percentage of LPRM signals calculated by verification test

The above conclusions depend on the reliability of the tests themselves. Currently there is at least one experimental evidence, which will be discussed below, that supports the validity of the tests. For the time being, we are strongly convinced that further investigation is needed to confirm or deny the applicability of the tests.

### 3.6 Analysis of detector signals for impacting

#### Some general information

The most thorough information regarding the damage caused by the guide tube vibrations comes from the inspection in 1992 (RA2-92) between cycles 17 and 18 ([27]). It is visually presented in the left part of Fig. 26 together with diagrams for the reactor power and core flow.

#### Comparison of measurements 9 and 10

Visual comparison of measurements 9 and 10 gives strong reasons to consider them as copies of each other because all LPRM signals of measurement 9 have almost the same time histories as compared to the corresponding LPRM signals of measurement 10. Fig. 27 shows a typical example. Nevertheless they are slightly different. This may be explained by assuming that these measurements arise from a common source (signal) which was differently preprocessed to yield the two measurements. Because of this we shall ignore measurement 10 since it is presumably a copy of measurement 9. It should be noted here that sometimes measurement 10 will still appear in some plots because of automatic plot generating procedures that we used.

#### Evaluation of the global (background) noise

As mentioned earlier, in the present study only the probably simplest wavelet analysis, the Haar transform was used to detect and quantify impactings. The Haar transformation

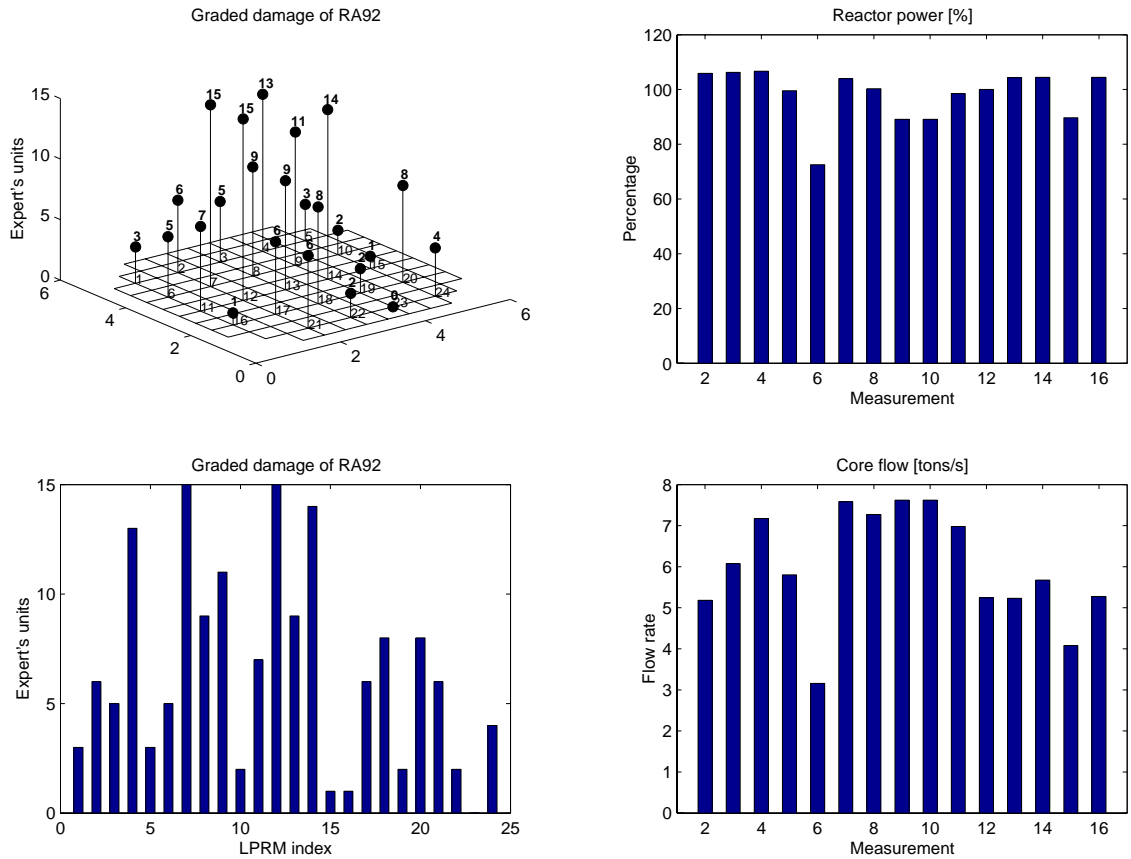


**Fig. 26.** Some general information about the measurements

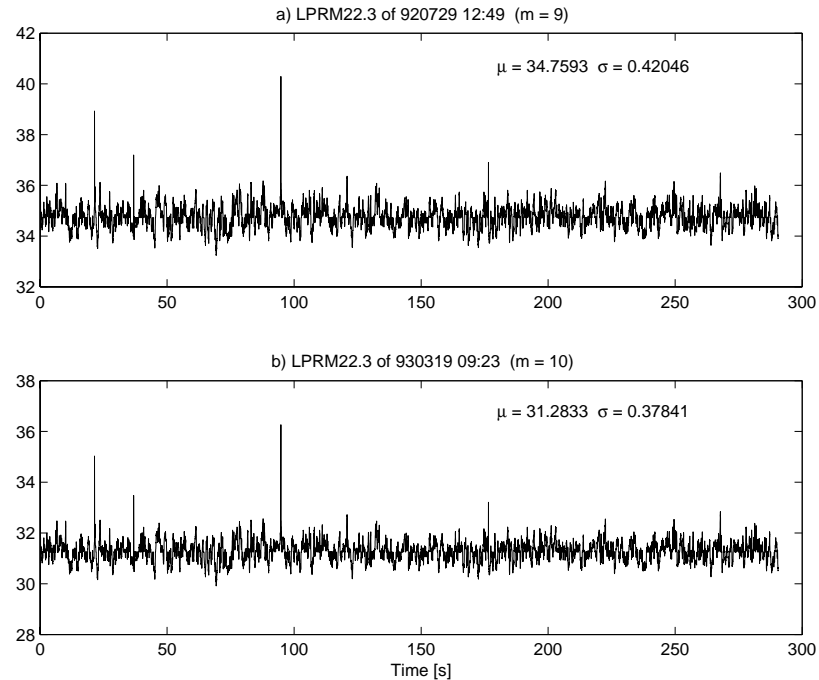


**Fig. 27.** Comparison of measurements 9 and 10

actually corresponds to only one level of decomposition. According to the theoretical model first we need to evaluate the global noise ingredient in the signals. This was achieved by first studying how certain characteristics of the high-pass filtered signal depend on the cut-off frequency. More specifically, the procedure involves the following steps:

- Select a cut-off frequency  $f$ ;

- Construct a high-pass filter  $HP_f$  corresponding to the frequency  $f$ ;
- Filter out low frequencies of the signal  $S$  to yield  $S_f = HP_f\{S\}$ ;
- Calculate characteristics of  $S_f$  such as standard deviation (std), kurtosis and so on;
- Plot the characteristics versus the frequency  $f$ .

Skewness was found to behave in a very similar way for all the signals. It decreases sharply at almost exactly 16 Hz. In other words, the filtered signal  $S_f$  has an almost perfect normal distribution with a cut-off frequency of 16 Hz or higher. This gives reasons to believe that the global noise (GN) component lies above the frequency  $f_{GN} = 16$  Hz. Fig. 28 supports this conclusion by showing several randomly selected signals. This makes evaluation of the threshold (77) well determined.

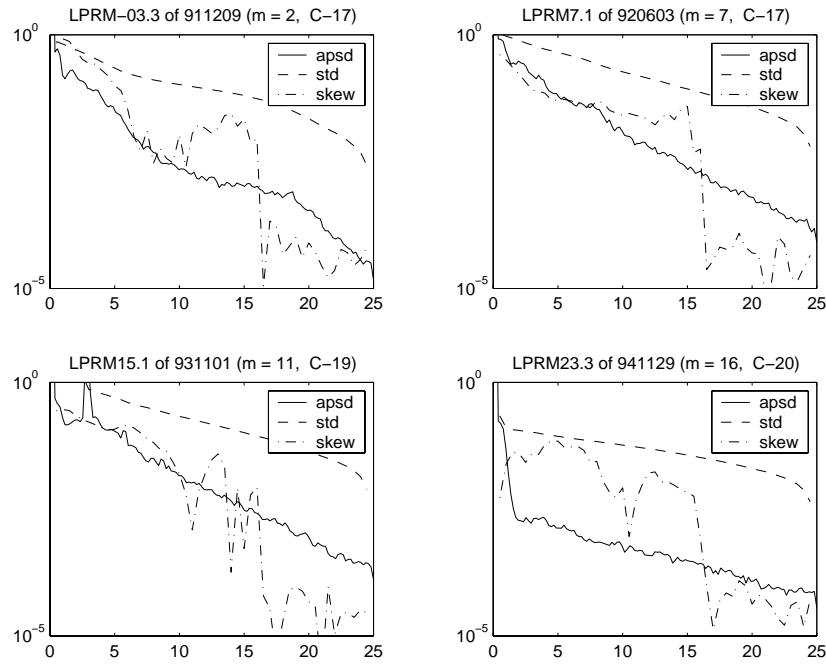


**Fig. 28.** Sharp decrease of skewness at around 16 Hz

### Impacting rate index

In order to quantify the severity of impacting, we define an impacting rate (IR) as the number of spikes detected by the Haar thresholding per unit time of observation. This definition is different from the one used in [23] where the vibration period was used as the unit of time. Typical examples of Haar-filtered signals, together with the IR values, are given in Fig. 29.

### Detection of impacting

In order to obtain a general overview of impacting, a string impacting index was calculated as a sum of the corresponding indices shown by the detectors in the same string. In addition, these indices were scaled relative to the maximal value observed in measurement 13 for LPRM-15. Because of its high importance, the core flow is also given in some relative units at position 26 marked also as F.

It is immediately seen that in cycle 19 (measurements 11 to 14), string #15 (see Fig. 30) shows an extremely high impacting rate in comparison to the other LPRMs.

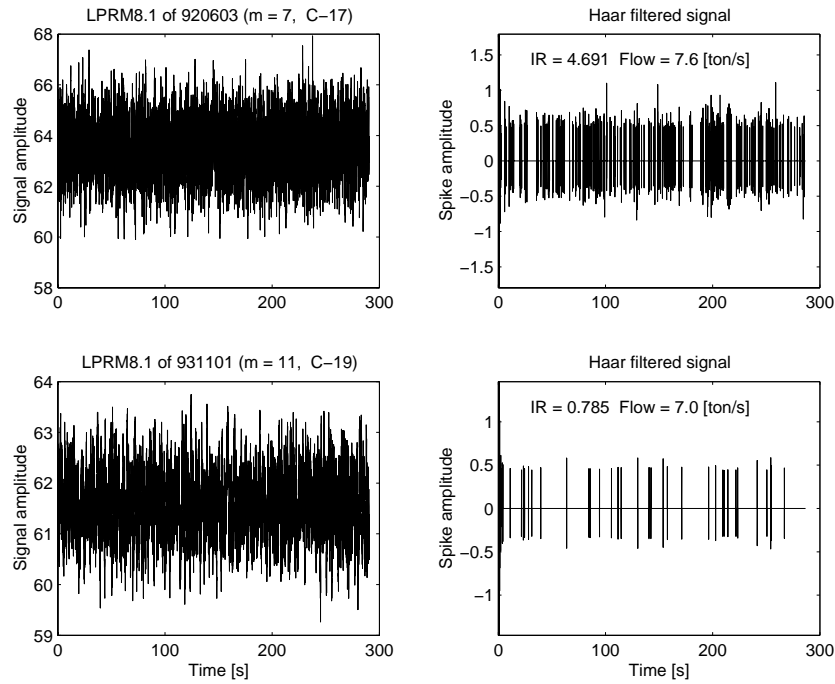


**Fig. 29.** Impacting rate index for two signals

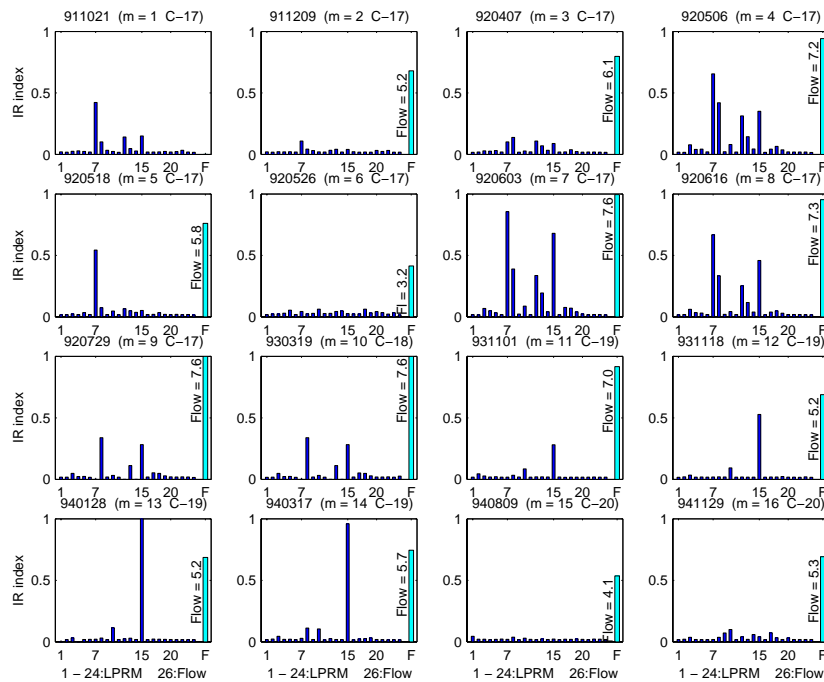


**Fig. 30.** Distribution of IR index

Moreover, one can clearly notice how the index grows with time despite the fact that the core flow at the end of the cycle is smaller than at the beginning of cycle ( $m = 10$ ,  $F = 7.6$ ). This has a natural explanation as a progressing worn-out of the vibrating tube. The revision RA2-92 (between cycles 19 and 20) did reveal a big hole in a fuel box around string #15.

A more complicated situation can be observed regarding cycle 17 ( $m=1$  to 9). Apparently string #7 shows, on the average, the highest IR index. Depending on the core flow, string #15 gives also a high impacting rate. In measurements with high flow rates ( $m = 4, 7, 8$ ;  $F = 7.2$  to  $7.6$ ) strings #8, 12 and 13 show relatively large IR indices. It should be

noted that the most vibrating or impacting strings (7,8,12,13) are located adjacent to each other.

Another important point to note is the fact that the damage revealed under inspection RA2-92 was accumulated during the whole cycle. Because of this an integral (cumulative) impacting index has been introduced as a sum of the corresponding IR indices during a cycle. Fig. 31 shows the cumulative IR index for cycle 17 together with the reported damage presented as negative values.

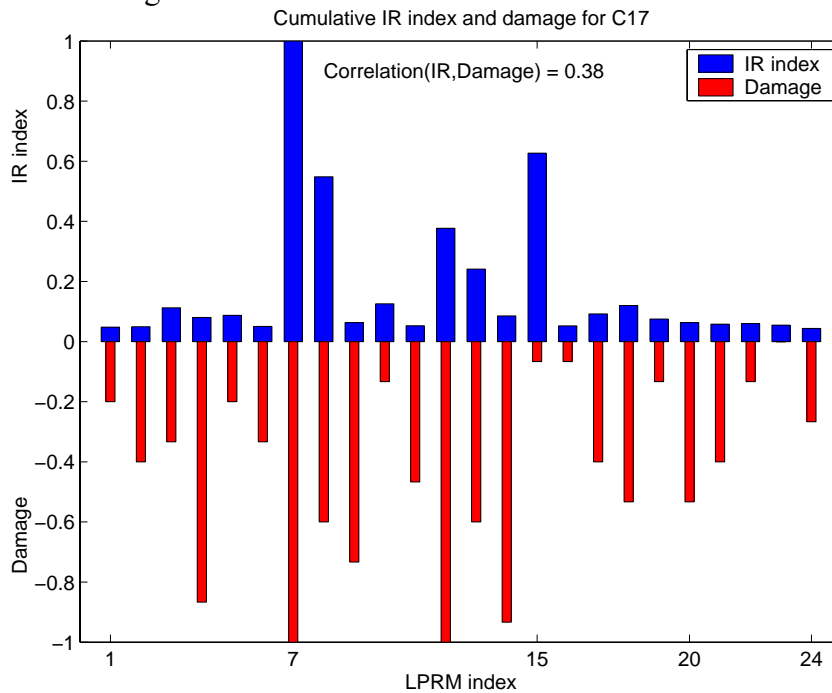


**Fig. 31.** Cumulative IR index and damage for cycle 17

As seen in the Figure, a good correlation was found between the wavelet result and the inspection-based damage rating for string #7 which was the most damaged one in this cycle. This is a significant result since the measurement data from this string were far from complete. In half of all cases (9 out of 18 measurements, i.e. 9 cycles for the two detectors in the string) signals coming from string 7 were discarded because of being BAD or N/A (not available) as it follows from Table V. The agreement for other tubes is also good on the average, but there are noticeable deviations for several strings.

One possible reason for the less than perfect correlation between the IR index and the damage found can be that the success of the detection may depend on the axial position of the detector. It was seen in earlier investigations where all four detector signals were available that there was a relatively large difference between the ability of the detector signals to indicate impacting [21]. In cases where the impacting occurs at an axial level far away from the two detectors used in the present study, the possibilities of impact detection are not optimal. This problem is often deteriorated further in the measurements where only one detector signal was available.

### Short overview of other indices

A number of other indices that might indicate impacting/vibration have been investigated. These were as follows (the abbreviations are used in the figures):

- mean - mean value;
- std - standard deviation;
- kurt - kurtosis;
- skew - skewness;
- DR - decay ratio;
- pp1 - power (amplitude) of the 1-st peak in APSD;
- ap1 - area under peak 1 in APSD;
- pp2 - power (amplitude) of the 2-nd peak in APSD;
- ap2 - area under peak 2 in APSD;
- pc1 - power (amplitude) of the 1-st peak in the coherence function between signal S1 (upper detector) and signal S2 (lower detector);
- ac1 - area under peak 1 in coherence;
- pc2 - power (amplitude) of the 2-nd peak in the coherence function;
- ac2 - area under peak 2 in coherence;
- va - vibrational amplitude calculated by the formula proposed in [28]:  
 $va = 3.28 \cdot \sqrt{\langle HP_f\{S_1\} \cdot HP_f\{S_2\} \rangle}$  with a cut-off frequency of 4 Hz;
- IR - impacting rate.

Fig. 32 gives an overview how the cumulative (i.e. summed over cycle 17) versions of the above listed indices correlate to the graded damage found during RA2-92.

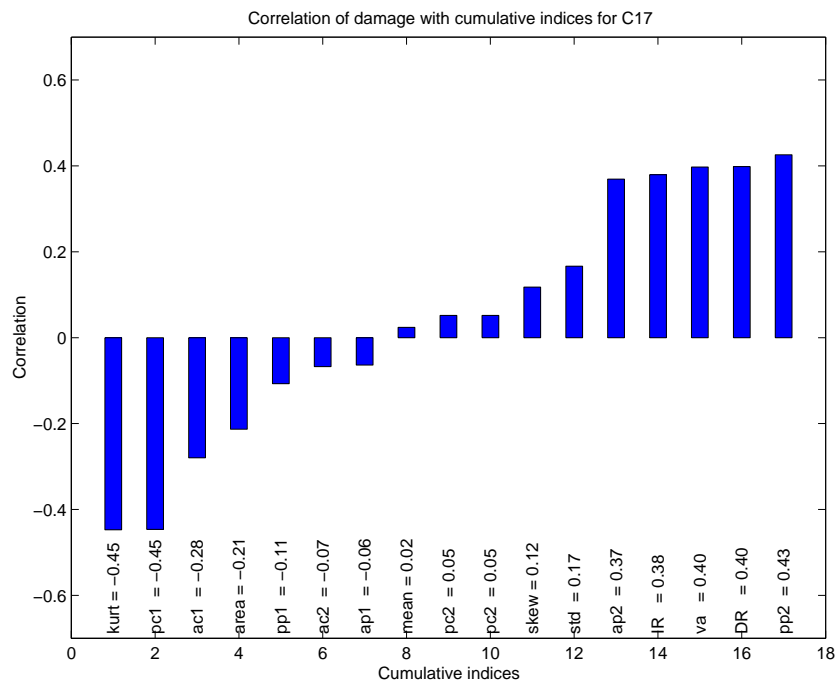


**Fig. 32.** Correlation of cumulative indices with the graded damage of RA2-92

It is interesting to note that the indicators kurtosis and peak 1 (pc1) in the coherence function give the strongest anti-correlation, -0.45, with the graded damage, whereas peak 2 in APSD (pp2) shows the greatest correlation, 0.43, with the damage. A comparable correlation, 0.38 to 0.40, is also shown by four other indices, namely ap2, IR, *va*, and *DR*. As is seen, the impacting rate does not give the highest correlation for this measurement series, although it gives the fourth highest one. As was mentioned earlier, the experimental data cannot be considered as complete, since some vital data, for example LPRM7.3, was missing, which might partially explain this fact.

Fig. 33 displays a distribution of the peak 1 area in APSD over all LPRMs and all measurements. Noting that string 7 does not show the strongest ap1 index one can assume that ap1 is an indicator of the string vibration rather than impacting. Another observation supporting this conclusion is a high correlation of the index with the core flow within a cycle. Finally, a sharp change in the character of the distribution of this indicator when the plug-in was made between cycles 17 and 18 points to the same conclusion.

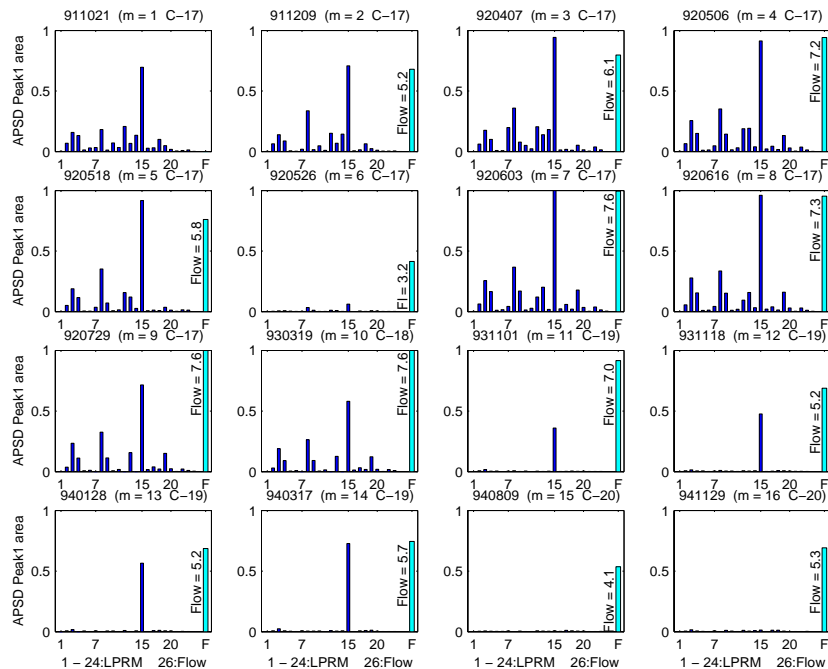


**Fig. 33.** Area under peak 1 in APSD

Fig. 34 shows a distribution of the area under peak 2 in the APSD over all LPRMs and all measurements. This peak occurs at a higher frequency and is generally much weaker as compared to ap1. Qualitatively, similar conclusions can be made about this parameter.

Fig. 35 shows the frequency of peak 1 in the different LPRM signals. Contrary to the previous figures, each string is represented here by two detector signals because it bears some important information.

First of all, one can easily notice a profound difference in the distributions before and after the plug-in. After the holes at the lower tie plate had been plugged, the core flow became less turbulent and most of the sensors detect one and the same frequency. Moreover there is a considerable difference between the upper and low detectors. As a rule, the lower ones detect a unique frequency, whereas the upper sensors do not necessarily indicate the same frequency. This may be explained by the core flow becoming less regular and more

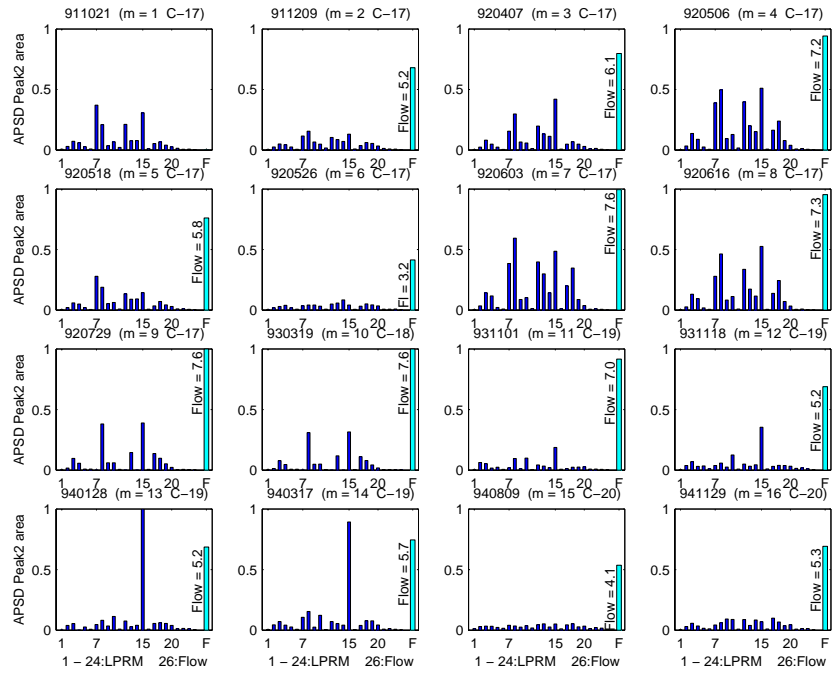


**Fig. 34.** Area under peak 2 in the APSD

turbulent while the coolant progresses upwards and the void content increases. A similar behaviour can sometimes be recognized for cycle 17,  $m = 6$ , when the core flow was lowest, 3.2 ton/s.

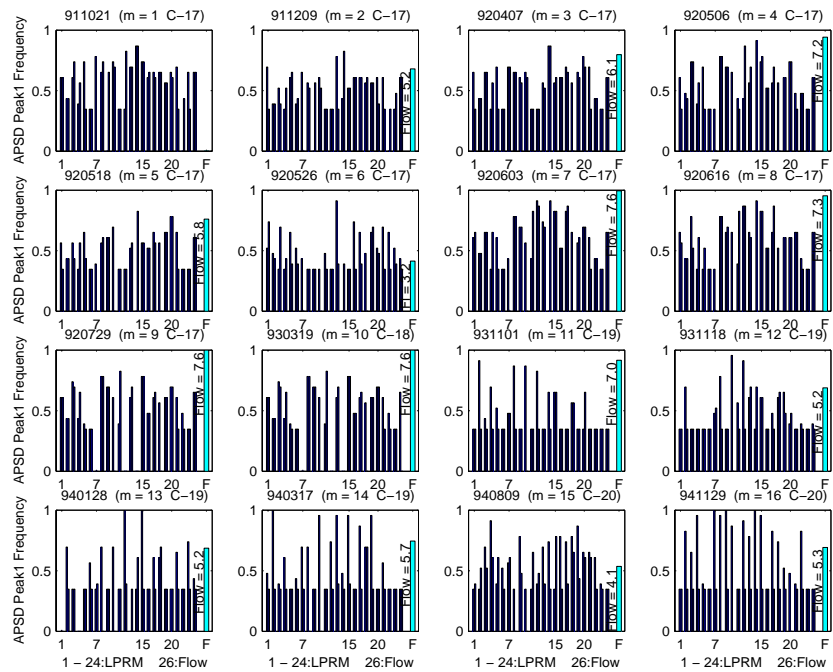


**Fig. 35.** Frequency of peak1 in APSD

Fig. 36 shows the frequency of peak 2 in the different LPRM signals. As before, each string is represented by two detector signals. Almost all sensors detect a unique frequency that does not depend on the core flow. One can conclude from this observation that the process responsible for this frequency is of a global nature.

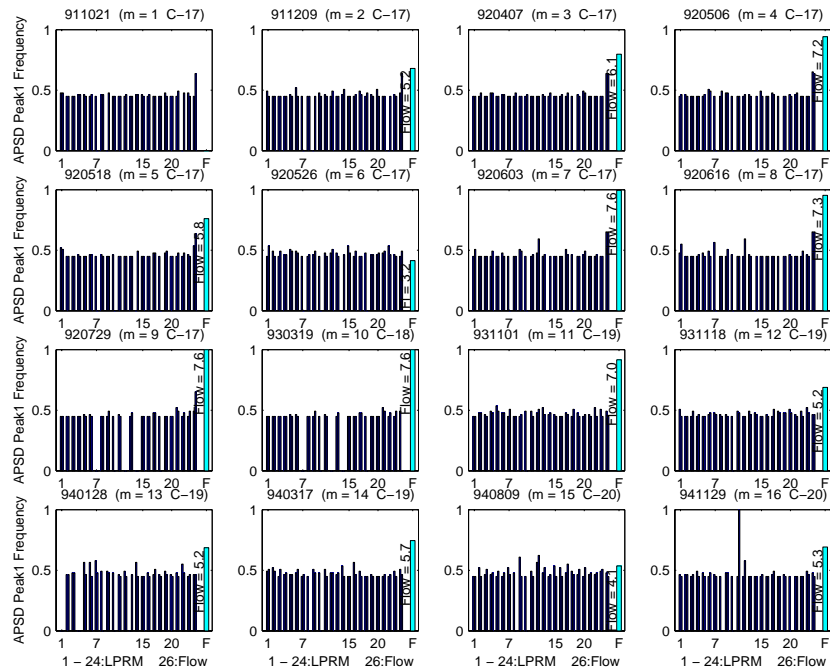


**Fig. 36.** Frequency of peak2 in APSD

### Burn-up of the detectors in string 16 during cycle 17

As reported in [27], the revision between cycles 17 and 18 (RA2-92) showed a significant burn-up and ageing of string 16 such that it was replaced. This experimental evidence gives an opportunity to watch the time history of the ageing detectors in string 16. Fig. 37 gives an important period in the time history, measurements 4 to 7.

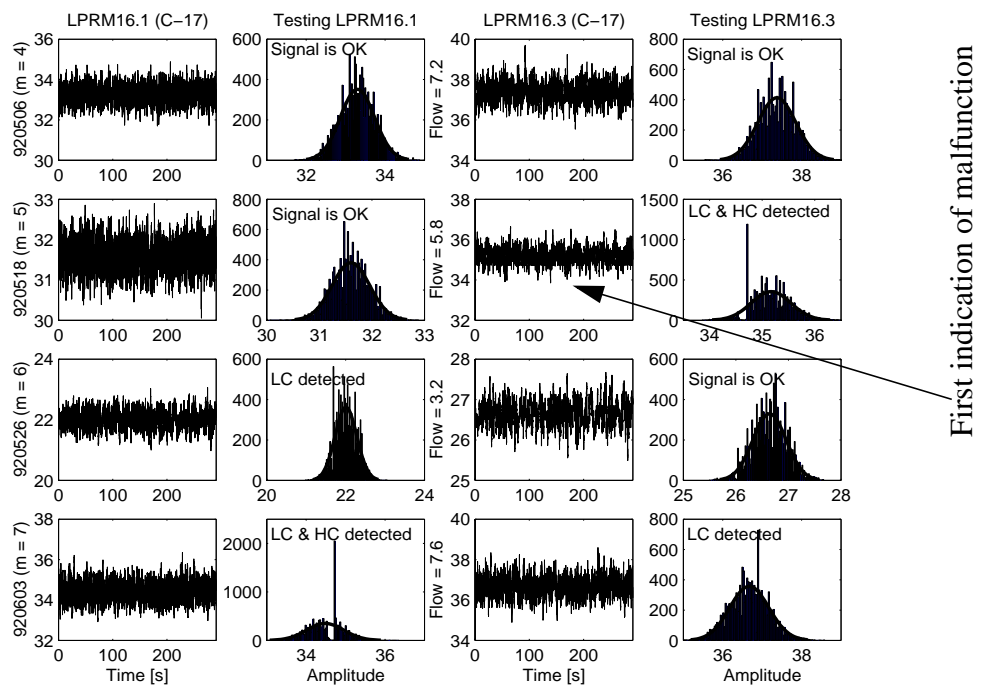


**Fig. 37.** Burn-up of the detectors in string 16 during cycle 17

Sometimes, the malfunction of a detector is well seen by a specific shape of the time series signal itself, as indicated in Fig. 37, which, in addition, says that more often this is not so visible. On the other hand, the proposed validation test, ZC, LC, and HC, firmly recognise these signals as deteriorated and mark them as being questionable up to the end of the cycle (see also Table V). It is not clear why the LPRM16.3 signal failed the test in measurement 5, then unexpectedly passed in measurement 6 and, finally, again failed in the following measurements of the cycle. Most probably, further adjustment and improvement of the validation test is needed.

### **3.7 Conclusions**

Analysis of the data taken in Oskarshamn 2 has lent an immense opportunity to test and develop tube impacting algorithms. In this stage first a thorough check of the detector signals was performed. Then, the impact detection technique based on the Haar transform was tested with all measurements. The analysis showed that for the most severe cases of impacting the Haar transform method appears to be very robust and reliable, such that it can be used for detection of impacting without calibration or resort to reference data. For less extreme cases the correlation between the impact rate parameter, deduced from the Haar transform and the actual damage was lower. Two possible explanations are that the measurement data were not complete due to sensor failures in several cases, and that access to detector signals close to the axial position of the impacting is important.

## Plans for the continuation

### In stage 8 we plan to include the following parts in the current R&D program:

- Continuation of the development of the noise simulator. The main point is to introduce nodal or finite elements methods for the space discretisation procedure, instead of the currently used finite difference method.
- Test of the localisation of the Forsmark local instability with real core data used in the noise simulator. In the present stage, data corresponding to an originally homogeneous core were used. In the next stage it is planned that the SIMULATE data, corresponding to the actual core loading in Forsmark-1, cycle 16 will be used. Preparations for obtaining of these data have already been started.
- Development of a phenomenological model for the reconstruction of the space dependence of the decay ratio in the Forsmark local instability event. During the instability in one half of the core the decay ratio was high ( $>0.9$ ) and nearly space-independent, and in the other half it was low ( $<0.6$ ) and also nearly constant in space. This behaviour could not be reconstructed by e.g. simulations with RAMONA. By assuming one or two local instabilities and possibly a global oscillation, and with a formerly developed expression for the decay ratio of a signal consisting of two or more oscillations with different decay ratios and amplitudes, we expect to be able to understand the spatial behaviour of the decay ratio. In the expressions, the amplitudes of the various components become now strongly space dependent, and we plan to use the noise simulator for the calculation of this space dependence.
- Test of wavelet methods other than the Haar transformation with the Oskarshamn 2 data. Some preliminary tests have already been performed in simulations. We have access to the wavelet toolbox of MATLAB with which various wavelet forms can be used. Since now we have a good knowledge about the content and the quality of the data, an effective comparative investigation of different wavelet transform techniques can be executed.

## Acknowledgement

This project was supported by the Swedish Nuclear Power Inspectorate, contract No. 14.5-000983-00156.

## REFERENCES

- [1] Pázsit I., Garis N. S. "Forskningsprogram angående härddiagnostik med neutronbrusmetoder." *Etapp 1. Slutrapport, SKI Rapport 95:14* (1995)
- [2] Pázsit I., Garis N. S., Thomson O. "Forskningsprogram angående härddiagnostik med neutronbrusmetoder." *Etapp 2. Slutrapport, SKI Rapport 96:50* (1996)
- [3] Pázsit I., Garis N. S., Karlsson J., Rácz A. "Forskningsprogram angående härddiagnostik med neutronbrusmetoder." *Etapp 3. Slutrapport, SKI Rapport 97:31* (1997)
- [4] Pázsit I., Karlsson J. K-H., "Research and Development Program in Reactor Diagnostics and Monitoring with Neutron Noise Methods." *Stage 4. Final Report, SKI Report 98:25* (1998)
- [5] Pázsit I., Karlsson J. K-H., Lindén P., Arjanov V. "Research and Development Program in Reactor Diagnostics and Monitoring with Neutron Noise Methods." *Stage 5.*

- Final Report, SKI Report 99:33 (1999)*
- [6] Pázsit I., Demazière C., Avdic S., Dahl B. “Research and Development Program in Reactor Diagnostics and Monitoring with Neutron Noise Methods.” *Stage 6. Final Report, SKI Report 00:28 (2000)*
  - [7] Edenius M., Ekberg K., Forssén B. H., Knott D. “CASMO-4, A Fuel Assembly Burnup Program, User’s Manual”, *Studsvik Report, Studsvik of America (1993)*
  - [8] Umbarger J. A. “TABLES-3, Library Preparation Code For SIMULATE-3, User’s Manual”, *Studsvik Report, Studsvik of America (1992)*
  - [9] Umbarger J. A., DiGiovine A. S., “SIMULATE-3, Advanced Three-Dimensional Two-Group Reactor Analysis Code, User’s Manual”, *Studsvik Report, Studsvik of America (1992)*
  - [10] Comsol AB “FEMLAB User’s Guide and Introduction, version 2.0”, *Comsol (2000)*
  - [11] Comsol AB “FEMLAB Reference Manual, version 2.0”, *Comsol (2000)*
  - [12] Nakamura, S. “Computational Methods in Engineering and Science With Applications to Fluid Dynamics and Nuclear Systems”, *Wiley Interscience, New York, pp. 89-92 (1977)*
  - [13] The Math Works “Using MATLAB, version 5”, *The Math Works, Inc. (1999)*
  - [14] Karlsson J. K-H., Pázsit I. “Study of the Possibility of Localising a Channel Instability in Forsmark-1” *SKI Report 98:28 (1998)*
  - [15] Karlsson J. K-H., Pázsit I. “Localisation of a channel instability in the Forsmark-1 boiling water reactor”, *Ann. Nucl. Energy* **26**, 1183-1204 (1999)
  - [16] Demazière C. “Analysis of the reactivity coefficients and the stability of a BWR loaded with MOX fuel”, *Proceedings of PHYSOR2000, Pittsburgh, Pennsylvania, USA (2000)*
  - [17] The Math Works “Signal Processing Toolbox User’s Guide, version 5”, *The Math Works, Inc. (2000)*
  - [18] Engström S. *Forsmark internal report FT-Rapport 97/135 (1997)*
  - [19] Söderlund M. *Forsmark internal report FT-Rapport 97/295 (1997)*
  - [20] Analytis G. Th., Hennig D., Karlsson J.K.-H. “The physical mechanism of core-wide and local instabilities at the Forsmark-1 BWR”, *Nuclear Engineering and Design* **205**, 91-105 (2001)
  - [21] Pázsit I., Glöckler O. “BWR Instrument Tube Vibrations: Interpretation of Measurements and Simulation”, *Ann. nucl. Energy* **21**, 759 - 786 (1994)
  - [22] Thomson O., Garis N. S. and Pázsit I. “Quantitative analysis of detector string impacting”, *Nuclear Technology* **120**, 71 (1997)
  - [23] Rácz A. and Pázsit I. “Detection of detector string impacting with wavelet techniques”, *Ann. nucl. Energy* **25**, 387-400 (1998)
  - [24] Thie J. A. Personal communication on the 18th IMORN, Prague, Czechoslovakia (1985)
  - [25] Pázsit I., Antonopoulos-Domis M., Glöckler O. “Stochastic aspects of two-dimensional vibration diagnostics”, *Prog. nucl. Energy* **14**, 165-196 (1984)

- [26] Mallat S. “A Wavelet Tour of Signal Processing”, *Academic Press, San Diego* (1998)
- [27] Karlsson J. K.-H., Bergdahl B.-G., Oguma R. “The guide tube vibrations at Oskarshamn-2 1991-1994”, *GSE Power Systems AB, GSE-01-006* (2001)
- [28] Bergdahl B-G. and Oguma R. “Investigation of In-Core Instrument Guide Tube Vibrations at Oskarshamn BWR Unit 2 Based on Noise Analysis”, *SKI Rapport 96:37* (1996)
- [29] Bergdahl B-G., Oguma R. “Experience of VIBMON: a BWR In-core Instrument Tube Vibration Monitor”, *Paper No 9.2, SMORN VII, Avignon, France, 19-23 June* (1995)